LBL-30717
Preprint

Lawrence Berkeley Laboratory
UNIVERSITY OF CALIFORNIA

Submitted to Nuclear Physics A

Mass Assymmetric Fission Barriers for ^{75}Br

D.N. Delis, Y. Blumenfeld, D.R. Bowman, N. Colonna,
K. Hanold, K. Jing, M. Justice, J.C. Meng, G.F. Peaslee,
G.J. Wozniak, and L. Moretto

May 1991

U. C. Lawrence Berkeley Laboratory
Library, Berkeley

FOR REFERENCE

Not to be taken from this room

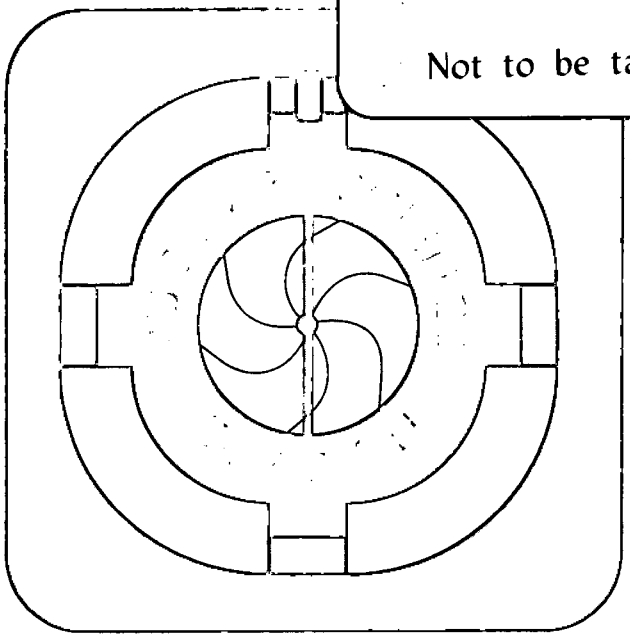

LBL-30717
Copy 1
Bldg. 50 Library.

Prepared for the U.S. Department of Energy under Contract Number DE-AC03-76SF00098

DISCLAIMER

This document was prepared as an account of work sponsored by the United States Government. While this document is believed to contain correct information, neither the United States Government nor any agency thereof, nor the Regents of the University of California, nor any of their employees, makes any warranty, express or implied, or assumes any legal responsibility for the accuracy, completeness, or usefulness of any information, apparatus, product, or process disclosed, or represents that its use would not infringe privately owned rights. Reference herein to any specific commercial product, process, or service by its trade name, trademark, manufacturer, or otherwise, does not necessarily constitute or imply its endorsement, recommendation, or favoring by the United States Government or any agency thereof, or the Regents of the University of California. The views and opinions of authors expressed herein do not necessarily state or reflect those of the United States Government or any agency thereof or the Regents of the University of California.

LBL-30717

Mass Assymmetric Fission Barriers for ^{75}Br

D.N. Delis, Y. Blumenfeld, D.R. Bowman, N. Colonna, K. Hanold,
K. Jing, M. Justice, J.C. Meng, G.F. Peaslee, G.J. Wozniak, and L. Moretto

Nuclear Science Division
Lawrence Berkeley Laboratory
University of California
Berkeley, Ca 94720, USA

This report has been reproduced directly from the best available copy.

This work was supported by the Director, Office of Energy Research, Division of Nuclear Physics of the Office of High Energy and Nuclear Physics of the U.S. Department of Energy under Contract DE-AC03-76SF00098

MASS ASYMMETRIC FISSION BARRIERS FOR ^{75}Br

D. N. Delis, Y. Blumenfeld[1], D. R. Bowman[2], N. Colonna, K. Hanold, K. Jing[3], M. Justice, J. C. Meng[3], G. F. Peaslee[2], G. J. Wozniak, and L. G. Moretto

Nuclear Science Division, Lawrence Berkeley Laboratory, 1 Cyclotron Rd, Berkeley, CA 94720

Abstract

Fragments with atomic numbers covering nearly the entire range of the mass-asymmetry coordinate ($4<Z<27$) were observed from the 5.0, 6.2, 6.9, 8.0, 10.2 and 12.7 MeV/A ^{63}Cu + ^{12}C reactions. Energy spectra and angular distributions show the presence of projectile-like and target-like components along with an isotropic component. The isotropic component appears as a Coulomb ring in the invariant cross-section plots indicating the presence of a binary compound decay which is confirmed by the coincidence data. Excitation functions were constructed for each Z value and a nearly complete set of mass-asymmetric barriers has been extracted for ^{75}Br. There is excellent agreement between the experimentally determined barriers and the finite-range model predictions.

---

1 Present address: Institute de Physique Nucleaire, Orsay, France
2 Present address: NSCL, MSU, East Lansing, MI 48844
3 Present address: Institute of Atomic Energy, Beijing, China

1.INTRODUCTION

Light particle evaporation and fission are the main modes of decay of a compound nucleus. They can be considered as the two limiting forms of a common process, whose underlying connection is provided by the mass-asymmetry coordinate. Light particle evaporation occurs at extreme mass asymmetries, while fission occurs at symmetry. Decay at intermediate mass asymmetries leads to the emission of complex fragments[1].

The probability of emission of a complex fragment depends on the barrier associated with that particular mass asymmetry. This barrier is associated with a "conditional saddle" with the constraint of a fixed mass asymmetry. As shown in Figure 1, the locus of all such conditional saddles defines a ridge line in the potential-energy surface of the nucleus[1]. A compound nucleus, confronted with this potential-energy ridge, can choose any asymmetry through which to decay. A continuum of trajectories can be envisaged, originating in the compound nucleus region, that reach up to the ridge and then descend towards the product region. The statistically favored trajectories are those passing through the lowest points of the ridge line. Since the nuclear shapes at the saddle are very indented, except for the heaviest nuclei, once a conditional saddle is negotiated the asymmetry should remain practically constant until scission. Thus, the probability of overcoming the ridge at the various asymmetries can be translated into mass distributions. The relationship between the yield Y and the conditional barrier B(z) for a given complex fragment is given approximately by $Y \propto \exp[-B(z)/T_z]$ where T_z is the saddle temperature[1]. Thus, the dependence of the conditional barriers on the asymmetry of the binary division determines the charge or mass distribution of the emitted fragments.

The shape of the ridge line depends on whether the fissility parameter x lies above or below the Businaro-Gallone point[2]. This point corresponds to the fissility parameter value at which the symmetric saddle point gains/loses stability against the mass-asymmetry coordinate. In the liquid drop model such a transition occurs at $x_{BG} = 0.396$ for zero angular momentum. The approximate dependence of the potential energy and the yield upon mass asymmetry is shown in Figure 2. For heavy nuclei, well above the Businaro-Gallone point, the ridge line presents a deep minimum at symmetry giving rise to the well known fission peak in the mass distribution. The ridge line also reaches a minimum at the largest asymmetries, producing the other well known decay mode, light particle evaporation. For light nuclei, below the Businaro-Gallone point, there is no longer a traditional fission saddle

point and the monotonically increasing ridge line towards symmetry implies the disappearance of fission as a process distinct from evaporation. Thus the fission peak vanishes and the mass distributions are "U" shaped with a minimum corresponding to symmetric division.

The precise form of the ridge line, or the dependence of conditional fission barriers upon mass asymmetry (Figure 2) requires the measurement of the entire mass distribution at various bombarding energies. In light systems these measurements are difficult because of the expected low yield for symmetric decay of the compound nucleus at the low excitation energies. Furthermore, one always needs to verify that the reaction occurs through the compound nucleus mechanism.

Experimental determinations[3,4,5] of symmetric fission barriers have played an essential role in the establishment of key features of nuclear models. For example, the ambiguity between the surface and Coulomb energy in the liquid-drop model has been resolved by fitting simultaneously both the ground-state and saddle-point masses in heavy nuclei[6]. Furthermore, shell effects for both the ground-state and saddle-point configurations have been verified by measurement of the fission barriers of nuclei in the vicinity of closed shells and in the actinide region, respectively[7].

In a large number of studies[8-13] experimental fission excitation functions were compared to statistical model calculations using the Rotating Liquid Drop Model (RLDM[14]) fission barriers. These studies concluded that the RLDM barriers needed to be reduced in order to fit the experimental data. Such a reduction in fission barriers agrees with the predictions of the Rotating Finite Range Model (RFRM[15-17]) which incorporates finite-range and surface-diffuseness refinements.

The RFRM barriers are lower than the RLDM barriers because the effect of the finite range of the attractive nuclear forces acting between the surfaces of the indented shape at the saddle point tends to lower the saddle point energies with respect to the liquid drop model, which assumes nuclei of sharp surfaces. The difference in the predicted barriers from the two models tends to decrease as one moves to higher values of the fissility parameter x and angular momentum as shown in Figures 3 & 4, respectively. This occurs because the indentation of the saddle shape decreases with increasing fissility parameter x and angular momentum, thus weakening the contributions of the attractive nuclear forces.

Calculations using the RFRM barriers have had good success in reproducing fission excitation functions obtained in heavy ion reactions ($A > 100$)[18,19]. The RFRM[17] has also

been successful in reproducing zero-angular momentum conditional barriers associated with the emission of complex fragments in ^{3}He induced reactions[20]. In order to extend the validity of the RFRM, a study of light nuclei (A<100) is desirable, since in this mass region the RFRM conditional barriers are 10 MeV or more lower than the corresponding RLDM barriers. This difference can be clearly seen in Figures 3 & 4 where the predicted fission barriers for J = 0 as a function of Z^2/A and for A = 75 as a function of angular momentum J of the compound nucleus are shown. The upper curve is calculated with the RLDM and the lower with the RFRM. The barriers and the finite range corrections are very large in the vicinity of A ≈ 50-100 and decrease as the mass or the angular momentum of the compound nucleus increases (see Figures 3 & 4).

The major objective of the present work is to provide, for the first time, a complete set of experimental asymmetric fission barriers for a single nucleus, against which macroscopic models can be tested. In this paper we present a nearly complete experimental ridge line of conditional barriers at zero angular momentum for ^{75}Br, obtained by studying complex fragment emission from the reaction ^{63}Cu + ^{12}C at six different bombarding energies (E = 5.0, 6.2, 6.9, 8.0, 10.2, 12.7 MeV/A). Early results of this study have been reported in Ref. 21.

The organization of the paper is as follows: The experimental details are given in Section 2. In Section 3, the results of the experiment are presented and the separation of complex fragments of compound nucleus (CN) origin from the deep-inelastic component is discussed. The experimental charge distributions compared to statistical model calculations and the extracted barriers are presented in Section 4. Finally the conclusions of this work are presented in Section 5.

2. EXPERIMENTAL METHOD

The experiment was performed at the 88-Inch Cyclotron of the Lawrence Berkeley Laboratory. Copper vapor was produced in a high temperature oven and introduced into an electron-cyclotron resonance source, where the Cu atoms were ionized. The ionized atoms were then injected into the cyclotron and accelerated to the desired energy. Rapid beam energy changes were accomplished by accelerating different charge states at the same mainfield setting. By keeping the mainfield constant, the settings for the transport line to the

experiment could be left unchanged. In addition, scaling the injection voltage with the charge state leaves the injection line settings constant[22] as well.

The ^{63}Cu beam impinged on a ^{12}C target of 0.5 mg/cm^2 thickness. The thin target ensured that the energy loss of the fragments within the target was small. Fragments were detected in two position-sensitive ΔE-E quad telescopes placed on either side of the beam. Each quad unit consisted of four separate gas-silicon telescopes. The active area of each telescope subtended 5 degrees both in-and out-of-plane. The gas ionization detectors served as ΔE detectors and were operated with isobutane gas at a pressure of 30 torr. The E detectors in each telescope unit were 5 mm thick silicon detectors with a resistive layer on the front to determine the position of a detected fragment. The telescopes were position sensitive in two dimensions. The in-plane position signal was obtained from the voltage division across a Pd resistive layer (5 KΩ) evaporated on the front surface of the Si detector. The out-of-plane position was determined from the drift time of the electrons in the gas ionization chamber. Using these telescopes, the energy, the atomic number, the in-plane and out-of-plane angles could be determined for each fragment that traversed the ΔE and stopped in the E detector.

These quad-telescope detectors covered an angular range of 24.8^0 in-plane, with a separation between the active edges of adjacent telescopes of 1.6^0. Measurements were initially performed with the detectors positioned to cover the angular range from 4^0 to 28.8^0. The detectors were then moved by 3^0, to allow fragments to be detected at angles which were initially located in the dead areas between adjacent telescopes. In this way, complete and continuous angular distributions were obtained for constructing invariant cross section diagrams with a relatively small amount of beam time.

The atomic number of the detected particles was determined from the measured ΔE and E values. An example of a ΔE-E map illustrating the range of fragments observed and the Z resolution achieved is shown in Figure 5.

The energy calibration of the Si detectors was obtained using several elastically scattered projectiles from a 1 mg/cm^2 Au target. Calibration points were obtained with beams of ^{18}O, ^{20}Ne, ^{37}Cl, ^{40}Ar and ^{63}Cu with energies ranging from 5.0 to 12.7 MeV/A. The gas ionization chambers were also calibrated at the same time. Measurements of the residual energy of the elastically scattered beam particles with and without gas in the ionization chamber, allowed the energy loss within the gas section to be deduced. These energy losses were used as calibration points. Corrections were made for energy losses in

the mylar window of the ionization chamber and in the Au absorber foils used for suppressing electrons and X-rays. The energy calibrations were accurate to ± 1%. Corrections were made for the pulse-height defect using the systematics of Moulton[23].

The position calibration was determined with a mask, consisting of a matrix of 2.5 mm diameter holes separated by 5 mm, that could be lowered into position remotely. The typical position resolution obtained was $\pm 0.2^0$. To obtain absolute cross sections, the beam charge was collected in a Faraday cup and integrated with an appropriate charge-integration module. This Faraday cup integration setup was calibrated from the measurements of Rutherford scattering on a ^{197}Au target with thickness of 1 mg/cm^2. Inclusive and coincidence events were recorded on magnetic tape and analyzed off-line.

3. RESULTS

3.1 Velocity diagrams.

The reaction was studied in reverse kinematics, namely the heavier ^{63}Cu nucleus was the projectile and the ^{12}C the target. The advantages of this technique can be seen by examining the kinematics diagram in Figure 6. In this figure the velocity of the source of the complex fragments is represented by the vector V_s. In the present reaction V_s represents the velocity of the compound nucleus, while V_e represents the velocity of the complex fragment emitted in the center of mass from the binary decay of the compound nucleus. V_e has a rather well defined value determined mostly by the Coulomb repulsion between the two decay products. The locus of the emission velocities for a particular complex fragment is represented by the circle. V_a and V_b are the velocities of the fragments observed at a laboratory angle θ. The high velocity solution (V_a) corresponds to the forward emission in the center of mass and the low velocity solution (V_b) corresponds to the backward emission in the center of mass. In Figure 5 one clearly sees the upper and lower kinematic ridges associated with the binary decay of a fast-moving compound nucleus. The upper and the lower ridges correspond to fragments emitted forward and backwards in the c.m. system, respectively.

Isotropic emission of complex fragments in the reaction plane is characteristic of the decay of a compound nucleus. To determine the existence of an isotropically emitting source and its velocity, the laboratory energy spectra were transformed into cross-section plots in velocity space. The velocity V of each fragment was calculated from its mass and

kinetic energy. When the excitation energy per nucleon E/A of the fragments was greater than 1 MeV their mass A was determined from the empirical formula[24] $A = 2.08Z + 0.0029Z^2$ where Z is the measured atomic number of the fragment. For fragments whose excitation energy per nucleon was less than 1 MeV, their mass A was determined from the relation $A = (A_{CN}/Z_{CN})Z$ where A_{CN} and Z_{CN} are the mass and atomic number of the compound nucleus. Both formulas predict the same values of mass within 0.3 mass-units over the range $4 < Z < 26$. In Figures 7 & 8 we present the cross section $\partial^2\sigma/\partial V_{\parallel}\partial V_{\perp}$ plotted in the $V_{\parallel}$-$V_{\perp}$ plane for representative complex fragments. For $Z > 8$ these plots show an isotropic ring of high cross-section (isotropic Coulomb ring). The width of the ring is broadened by sequential evaporation of light particles and fluctuations of the Coulomb energy near the scission point arising from thermal fluctuations in various collective degrees of freedom[1,25,26]. The observed Coulomb rings correspond to the emission of fragments with Coulomb-like velocities from a single source with a well defined laboratory velocity. These rings have been previously observed[24-27] and are indications of fully relaxed binary decays associated with either deep inelastic processes or compound nucleus emission. The center of each ring defines the laboratory velocity of the source system (compound nucleus or composite system) and the radius corresponds to the emission velocity with which the complex fragments are emitted in the source frame. For the lighter fragments (Z = 6 & 8 see Figure 7), the isotropic component is still visible at the forward angles. However, at backward angles, the isotropic component is masked by the stronger target-like deep inelastic component, which is backward peaked in reverse kinematics.

3.2 Source velocities

The source and emission velocities for each atomic number were obtained from its Coulomb ring by determining its center and average radius. The velocity corresponding to the center of each ring is the experimental source velocity (V_S). For the four highest energies the source velocity vs. fragment atomic number are shown in the upper portions of each quadrant of Figure 9. The experimental source velocities show very little dependence on the fragment Z-value confirming that all fragments are emitted by the same source. These source velocities agree closely with the velocities expected for complete fusion V_{cf}, which are indicated in Figure 9 by the solid lines.

The statistical error in V_S is smaller than the size of the symbols used in Figure 9. The large single error bar shown for each bombarding energy in Figure 9 gives an estimate

of the systematic error arising from the energy calibration of the detectors and the mass parameterization. The fact that the data points tend to lie slightly below the V_{cf}, which is unphysical, is due to these systematic errors.

3.3 Emission velocities.

The average radii of the Coulomb circles or emission velocities (V_e) of the fragments are shown in the lower portions of each quadrant of Figure 9 (represented by the diamonds). The Coulomb nature of these velocities can be inferred both from their magnitude and from their nearly linear dependence upon atomic number. A calculation (solid line) of the Coulomb velocities based upon the Viola[28] systematics generalized to asymmetric divisions is also shown in Figure 9. Details of this calculation are given in the following section. The dashed lines are the first moments of the emission velocity distributions calculated with the statistical code GEMINI[25,26], which includes evaporation and angular momentum effects. The agreement between the data and the calculations is quite good and confirms that the emission velocities are Coulomb like and consistent with statistical emission.

Each emission velocity V_e is associated with a distribution that arises from the width of the Coulomb ring. The variances of these distributions for each fragment are plotted at the bottom of Figure 9 (open squares). The variances calculated with the statistical code GEMINI are also shown (stars) and reproduce quite well the experimental values.

3.4 Kinetic Energy Spectra.

The kinetic energy of the emitted fragment in the center of mass was calculated by the formula $E_{cm} = 1/2\ A\ (V)^2$ where A is the mass of the fragment (discussed in section 3.1) and V is the velocity of the fragment in the source frame. In particular V has a distribution whose peak value is V_e. The widths of the energy spectra arise from the widths of the rings that are associated with each V_e. Figure 10 shows the kinetic energy spectra for a typical light fragment (Z=5) at different angles in the center of mass. For light fragments such as Z = 5, there are contributions from both the isotropic and deep inelastic components. At the most forward angles, the spectra show only the isotropic component. At more backward angles there are additional contributions from the deep-inelastic component. This can be clearly seen in Figure 10 where the maximum and the width of the energy spectra increase in value with increasing angle because of the additional deep-inelastic component.

Kinetic energy spectra could be constructed for most Z-values by integrating over the center of mass angular range covered by our detectors (20^0 to 160^0). In order to avoid contamination from the deep inelastic component, the spectra of the lighter fragments ($Z < 10$) were integrated between the angles of 20^0 and 80^0. Energy spectra for representative Z-values are shown in Figure 11 for the 8.0 MeV/A $^{63}Cu + ^{12}C$ reaction.

The first (Xs) and second (crosses) moments of the energy spectra in the center of mass were extracted for each Z-value and are plotted in Figure 12. The Coulomb-like behavior of the first moments of these distributions can be inferred through a simple comparison. A calculation of the Coulomb energy based on an initial scission configuration of two spheres is shown by the solid curve. Since the Viola systematics[28] has been compiled for symmetric fission, we have generalized it for asymmetric decay by solving for the radius parameter r_0 in $E_{Viola} = 1.44 * Z_1 * Z_2 / r_0 (A^{1/3} + A^{1/3})$ with $Z_1 = Z_2$, $A_1 = A_2$. The extracted r_0 was then used to calculate the kinetic energy released for asymmetric decay where $Z_1 \neq Z_2$ and $A_1 \neq A_2$. Although there is a significant deviation from the calculations for the lighter fragments, the overall agreement indicates that the kinetic energy is Coulomb like. The kinetic energies predicted by the statistical code GEMINI, represented by the diamonds, are also shown in the figure.

The second moments (crosses) of the experimental kinetic energy distributions, also shown in Figure 12 increase with decreasing fragment charge. An overall increase in the widths is observed as a function of the bombarding energy. The widths of the energy distributions arise from various causes. They are partly due to fluctuations in the Coulomb energy near the scission point arising from thermal shape fluctuations[1,25,26]. At the higher bombarding energies, the evaporation of light particles from the CN before and after scission also contributes to the width. The squares at the bottom of Figure 12 are the widths of the kinetic energies as calculated by GEMINI which reproduces both the magnitude and trend of the experimental widths.

3.5 Angular distributions.

As has been pointed out in previous work[27,29-32], and in the previous section, along with the isotropic component, deep-inelastic (target-like and projectile-like) components also appear in these reactions. The experimental angular distributions $d\sigma/d\theta_{cm}$ in the frame of the source system allow one to distinguish and measure the contribution of the various components (see Figures 13 & 14).

For intermediate Z-values the isotropic component dominates and the distributions are flat over the measured angular range, indicating that these fragments are emitted isotropically in the reaction plane. For fragments with Z<10, the distributions are peaked at backward angles due to the presence of an additional target-like component. The projectile-like component is associated with the slight forward peaking of the distributions for Z>23. Fragments larger than the projectile were not observed in the angular range studied due to their strong kinematic focusing to very small angles. Such fragments were lost along the beam direction, since our detectors were limited to angles greater than the critical angle, θ_{crit}.

3.6 Cross-sections.

At all bombarding energies an isotropic component can be seen for most fragment Z-values. Angle-integrated cross sections for the isotropic components were determined from the average value $d\sigma/d\theta$ of the flat regions in the angular distributions. When no flat region was obseved in the angular distributions, a constant equal to the minimum value of $d\sigma/d\theta$ was taken as an upper limit for the isotropic cross-section. The non-isotropic components, which we identified with quasi- and deep-inelastic reactions, are concentrated in the general neighborhood of the target and projectile. For all six energies the measured charge distributions of the isotropic component are shown in Figure 15 while the corresponding excitation functions are shown in Figure 16.

The measured charge distribution of the isotropic component shows the characteristic U-shape associated with the decay of a compound system below the Businaro-Gallone point. The change of the absolute cross-section as well as the evolution in shape of the charge distribution as a function of bombarding energy are shown in Figure 15.

The observed flattening of the charge distributions with increasing energy can be explained by the increase in the temperature of the system which tends to make all of the decay channels more equally probable as predicted by the equation $\Gamma_Z \propto \exp(-B_Z/T)$.

The complex fragment cross sections calculated with the statistical model code GEMINI are also shown in Figure 15. This code calculates the decay of a compound nucleus. All possible binary decays from light particle emission to symmetric division are considered. After each binary division, further decay of the resulting excited fragments is followed until all of the available excitation energy is exhausted. The barriers used in these calculations were obtained from the RFRM using a two spheroid parameterization for the shape of the conditional saddle-point configurations[15,33]. This parameterization generates

conditional barriers which are within 2 MeV of the saddle point energies calculated with more realistic shape parameterizations[15] for A=110. To correct for this difference, the two-spheroid saddle point energies are scaled by a constant factor for all mass asymmetries and angular momentum. The scaling factor is chosen so that for symmetric division, the scaled saddle-point energy was equal to the value calculated with the more realistic shape parameterization by Sierk[15,33]. The cross-section is integrated over ℓ waves up to a maximum ℓ value that provides the best fit to the experimental charge distributions. In all cases the quality of the fit is very good and the fitted values of ℓ_{max} are close to those predicted by the Bass model[34,35] (See Table 1).

3.7 Coincidence Data

Events in which coincident fragments were detected on opposite sides of the beam axis were analyzed. Practically no coincidences between telescopes on the same side of the beam axis were observed. This is consistent with the predominantly binary nature of the complex fragment events and conservation of momentum. Plots of the total detected charge $Z_1 + Z_2$ are shown in Figure 17. Essentially all of the total charge Z_{CN} of the CN is detected in the two fragments, which confirms the binary nature of the reactions. The small difference between Z_{CN} and the detected charge $Z_1 + Z_2$ determines the amount of charge particle evaporation from the hot primary fragments. The total charge for ^{75}Br is 35; the average total charge loss at the highest energies is about 2 units smaller and decreases to less than half a unit at the lower energies.

4. CONDITIONAL BARRIERS

The excellent agreement between model calculations and experimental data (Figure 15) suggests that the conditional barriers used in the statistical code GEMINI are quite close to the actual values. In order to obtain the best values of these barriers as well as their sensitivity to a variety of parameters, the experimental excitation functions have been fitted with functions obtained from a transition-state method following the Bohr-Wheeler formalism[1,36,37,38] and from the Weisskopf[39] theory (light particle emission). In the transition state theory, the reaction coordinate is determined at a suitable point in coordinate space, (typically at the saddle point) and the decay rate is identified with the phase space flux across a hyper plane in phase space passing through the saddle point and perpendicular

to the fission direction. The decay width for first chance emission of a fragment of charge Z is expressed as:

$$\Gamma_z = \frac{1}{2\pi\rho(E-R_{sph})} \int_0^{E-B_z} \rho(E - B^z_{eff} - \varepsilon)d\varepsilon \tag{1}$$

where $\rho(E-R_{sph})$ is the compound nucleus level density, $\rho(E - B^z_{eff} - \varepsilon)$ is the level density at the conditional saddle with kinetic energy ε in the decay mode and B^z_{eff} is the effective fission barrier defined as $B^z_{eff} = B_z + R_{sad}$, with B_z being the conditional barrier for zero angular momentum. R_{sph} and R_{sad} are the rotational energies of the spherical nucleus and rotating saddle point, respectively. The neutron and proton widths can be written as:

$$\Gamma_n = \frac{2mR^2g'}{\hbar^2 2\pi\rho(E-R_{sph})} \int_0^{E-B_n} \varepsilon\rho(E - B^n_{eff} - \varepsilon)d\varepsilon \tag{2}$$

and

$$\Gamma_p = \frac{2mR^2g'}{\hbar^2 2\pi\rho(E-R_{sph})} \int_0^{E-B_p} \varepsilon[1 - \frac{\varepsilon_c}{\varepsilon}]\rho(E - B^p_{eff} - \varepsilon)d\varepsilon \tag{3}$$

respectively, where $\rho(E-R_{sph})$ is the level density of the excited compound nucleus, $\rho(E - B^n_{eff} - \varepsilon)$ and $\rho(E - B^p_{eff} - \varepsilon)$ are the level densities of the residual nucleus after neutron or proton emission, respectively. ε is the energy of the emitted particle (neutron or proton), m its mass, g' its spin degeneracy, R the radius of the nucleus from which its being emitted, and ε_c is the Coulomb barrier for proton emission. B^n_{eff} and B^p_{eff} are the effective neutron and proton barriers defined as $B^n_{eff} = B_n + R_{sph}$ and $B^p_{eff} = B_p + R_{sph}$, where B_n is the neutron binding energy and B_p is the proton binding energy.

As shown in equation 1, the angular momentum dependence of Γ_z has been obtained by the addition of the rotational energy $R_{sad} = \hbar^2 \ell(\ell+1)/2I$ to the conditional barrier for zero angular momentum B_z, where I is the moment of inertia about an axis perpendicular to

the nuclear symmetry axis of the nucleus at the conditional saddle point. Such treatment of the angular momentum is adequate since the calculated moment of inertia of the saddle point is virtually constant[15] over the range of angular momentum considered here.

The formalism presented above requires the use of specific level density expressions in the widths Γ_n, Γ_p and Γ_Z. It is mainly in these quantities that all the physical information concerning the nucleus at the saddle point and the residual nucleus after light particle emission is contained. For the level density we have used the expression $\rho(E) \propto \exp[2(aE)^{1/2}]$ where E is the excitation energy of the system and a is the level density parameter, which is related to the single particle level density g by the expression $a = \pi^2/6\, g$. The level density parameter a has been given the value $a = A/9$.

The maximum angular momenta ℓ_{max} used in the calculations were not treated as free parameters for each individual fit (for each Z). Instead they were chosen to minimize the χ^2 of all the fits simultaneously. The angular momentum distribution following fusion σ_ℓ was parametrized using a Fermi distribution[18,19,40]:

$$\sigma_\ell = \frac{\pi\lambda^2(2\ell + 1)}{1+\exp[\frac{\ell - \ell_{max}}{\delta\ell}]} \tag{4}$$

where $\delta\ell$ determines the diffuseness of the distribution and ℓ_{max} is the maximum angular momentum. The value of $\delta\ell$ was chosen to be 4. This value is close to those needed to fit experimental fission excitation functions at low bombarding energies[13,18]. The expression used in evaluating the cross section for a given fragment was given by : $\sigma_Z = \Sigma\ \sigma_\ell\ P_Z(\ell)$ where $P_Z(\ell)$ is the probability of emitting a complex fragment. In the expression used for $P_Z(\ell)$, we have included second and third chance emission. The total decay width was taken to be equal to $\Gamma_T = \Gamma_n + \Gamma_p + \Gamma_Z$ where Γ_n, Γ_p, Γ_Z are the decay widths for neutron, proton and complex fragment emission, respectively. The decay width for alpha emission was not included in the total decay width. This is reasonable, since in this mass region $\Gamma_n + \Gamma_p >> \Sigma_{Z>1}\, \Gamma_Z$, as predicted by GEMINI.

The excitation functions were analyzed by a means of a two parameter fit. One of these parameters was the conditional fission barrier and the other the ratio of the level density parameters at the saddle point and for the residual nucleus after neutron decay (a_Z/a_n). The fits are shown in Figure 16 by the solid lines. Excellent agreement is obtained for all Z values. The quality of the fits is also shown in Figure 18 where charge distributions obtained from the experiment (diamonds) are compared with those obtained from the fits (solid lines). The agreement between the data points and the calculations for

all six energies is quite good. The L_{max} values extracted from the the fits (Figure 16) are nearly identical with the values used (Figure 15) in GEMINI and about $2\hbar$ lower than the Bass model predictions, as can be seen from Table 1.

The extracted barriers are represented by the solid points in Figure 19. They increase as a function of mass asymmetry, peak at symmetry and then fall off. This is the trend expected for a system with A = 75 whose fissility parameter x = 0.28 lies well below the Businaro-Gallone point. The experimentally determined barriers are remarkably well reproduced by the RFRM[41] calculations (solid curve). On the other hand, the RLDM (dashed curve) overestimates the barriers by almost 15 MeV. This large disagreement justifies the inclusion of finite range and surface diffuseness refinements in the RFRM.

The values of a_z/a_n extracted from the fits span the range of values from 0.90 to 0.98 and most values are centered around 0.91. The ratio a_z/a_n decreases as a function of mass asymmetry with a minimum around symmetric splitting and then increases again. This behavior is not understood.

The extracted zero-angular momentum barriers (Figure 19, lower) and ratio of level density parameters (Figure 19, upper) are subject to several uncertainties. Thus the sensitivity of the fit was examined with respect to changes in the fitting parameters and possible uncertainties in the data. A variation of the level density parameter within reasonable limits (between A/8 and A/10) introduces an uncertainty in the extracted barriers and values of a_z/a_n of at most $\pm$ 2% for all values of Z without changing significantly the $\chi 2$ of each fit. In addition, a change of the diffuseness parameter $\delta\ell$ between 2 and 6 shifts the barriers by $\pm$ 1%. Similarly, a systematic variation of the measured cross sections (increased or decreased by 50% from the values shown in Figure 16, in order to allow for possible unexpected systematic errors) introduces an uncertainty of at most $\pm$ 2% in the extracted barriers and values of a_z/a_n. Thus, we assign a possible overall uncertainty of $\pm$ 3.5%.

The amount of charge loss by the fragments due to sequential evaporation has been determined from the $Z_1 + Z_2$ coincidences. The average total charge loss at the highest energy is about 2 units and it decreases rapidly to less than half a unit with decreasing energy. This small correction has not been applied to the abscissae of Fig. 19.

A check that our results are internally consistent can be made by comparing the barriers for complementary atomic numbers (atomic numbers whose sum is equal to the atomic number of the compound nucleus). From Table 1 one can see that the barriers for

complementary charges (e.g. B_Z for Z = 15 and B_Z for Z = 20) have almost the same value, within 1 MeV. Lighter fragments tend to have slightly lower barriers than their complementary partners. This difference may arise from the difficulty in identifying the heavier fragment atomic numbers at the lowest energies.

5. Conclusion

Complex fragments were detected in the reaction $^{63}Cu + ^{12}C$ at the bombarding energies of 5.0, 6.2, 6.9, 8.0, 10.2, and 12.7 MeV/A. From the measured kinetic energy, angular and velocity distributions, the observed complex fragment emission could be separated into two components. a) A component associated with the binary decay of the compound nucleus, which has an isotropic angular distribution in the reaction plane and covers the entire range of atomic numbers. b) A deep-inelastic and quasi-elastic component associated with the target-like and projectile-like fragments.

The isotropic component was found to result from the statistical binary decay of the compound nucleus formed in complete fusion reactions. The experimental cross sections and velocity distributions were well reproduced by statistical model simulations. A nearly complete ridge line of the potential-energy surface for ^{75}Br was experimentally obtained. The experimental barriers are peaked at symmetry and decrease towards both larger and smaller values of the mass asymmetry as is characteristic of systems below the Businaro-Gallone point. The small uncertainties of the extracted conditional barriers ($\pm$ 3.5%) and the remarkable agreement between the experimentally determined conditional barriers and those predicted by theory justify the incorporation of finite-range effects in the liquid-drop model.

Acknowledgement

This work was supported by the Director, Office of the Energy Research, Office of High Energy and Nuclear Physics, Division of Nuclear Physics, of the U.S. Department of Energy under Contract No. DE-AC03-76SF00098.

References

1) L.G. Moretto, Nucl. Phys. **A247** (1975) 211
2) U.L. Businaro and S. Gallone, Nuovo Cimento **1** (1955) 629 and **1** (1955) 1277
3) D.S. Burnett, R.C. Gatti, F. Plasil, B.P. Price, W.J. Swiatecki, and S.G. Thomson, Phys. Rev. **134** (1964) 952
4) G.M. Raispeck and J.W. Cobble, Phys. Rev. **153** (1967) 1270
5) L.G. Moretto, S.G. Thompson, J. Routti and R.C. Gatti , Phys. Lett. **38B** (1972) 471
6) W.D. Myers, Droplet Model of Atomic Nuclei (IFI Plenum, New York, 1977)
7) B.B. Back, O. Hansen, H.C. Britt, J.D. Garrett and B. Leroux, Physics and Chemistry of Fission, Vol. 1, I. A. E. A., Vienna (1974), p. 3
8) J.R. Huizenga, R. Chaundry, and R. Vandenbosch, Phys. Rev. **126** (1962) 210
9) M. Beckerman and M. Blann, Phys. Rev. **C17** (1985) 1615
10) F. Plasil, R.L. Ferguson, R.L. Hann, F.E. Obenshain, F. Pleasonton and G.R. Young, Phys. Rev. Lett. **45** (1980) 1615
11) M. Blann and T. Komoto, Phys. Rev. **C26** (1982) 472
12) D.J. Hinde, J.O. Newton, J.R. Leigh and R.J. Charity, Nucl. Phys. **A398** (1983) 308
13) R.J. Charity, J.R. Leigh, J.J.M. Bokhorst, A. Chatterjee, G.S. Foote, D.J. Hinde, J.O. Newton, S. Ogaza and D. Ward, Nucl. Phys. **A457** (1986) 441
14) S. Cohen, F. Plasil and W.J. Swiatecki, Ann. Phys. **82** (1974) 557
15) A.J. Sierk Phys. Rev. **C33** (1986) 2039
16) H.J. Krappe, J.R. Nix and A.J. Sierk, Phys. Rev. **C20** (1979) 992
17) A. J. Sierk, Phys. Rev. Lett. **55** (1985) 582
18) J. van der Plicht, H.C. Britt, M.M. Fowler, Z. Fraenkel, A. Gavron, J.B. Wilhelmy, F. Plasil, T.C. Awes and G.R. Young, Phys. Rev. **C28** (1983) 2022
19) F. Plasil, T.C. Awes, B. Cheynis, D. Drain, R.L. Ferguson, F.E. Obenshain, A.J. Sierk, S.G. Steadman and G.R. Young, Phys. Rev. **C29** (1984) 1145
20) M.A. McMahan, L.G. Moretto, M.L. Padgett, G.J. Wozniak, L.G. Sobotka and M.G. Mustafa, Phys. Rev. Lett. **54** (1985) 1995
21) D.N. Delis, Y. Blumenfeld, D.R. Bowman, N. Colonna, K. Hanold, K. Jing, M. Justice, J.C. Meng, G.F. Peaslee, G.J. Wozniak and L.G. Moretto, Z. Phys. A, in press
22) D.J. Clark and G.J. Wozniak, Nucl. Instr. & Meth. A295 (1990) 34
23) J.B. Moulton, E.J. Stephenson, R.P. Schmitt and G.J. Wozniak, Nucl. Instr. & Meth. **157** (1978) 325
24) R.J. Charity, M.A. McMahan, G.J. Wozniak, R.J. McDonald, L.G. Moretto, D.G. Sarantites, L.G. Sobotka, G. Guarino, A. Pantaleo, L. Fiore, A. Gobbi and K. Hildenbrand, Nucl. Phys. **A483** (1988) 371
25) R. J. Charity, D.R Bowman, Z.H. Liu, R.J. McDonald, M.A. McMahan, G.J. Wozniak, L.G. Moretto, S. Bradley, W.L. Kehoe and A.C. Mignerey, Nucl. Phys. **A476** (1988) 516

26) R.J. Charity, K.J. Jing, D.R. Bowman, M.A. McMahan, G.J. Wozniak, L.G. Moretto, N. Colonna, G. Guarino, A. Pantaleo, L. Fiore, A. Gobbi and K.D. Hildenbrand, Nucl. Phys. **A511** (1990) 59
27) H. Han, K.X. Jing, E. Plagnol, D.R. Bowman, R.J. Charity, L. Vinet, G.J. Wozniak, and L.G. Moretto, Nucl. Phys. **A492** (1989) 138
28) V.E. Viola, K. Kwiatkowski and M. Walker, Phys. Rev **C31** (1985) 1550
29) G.J. Mathews, J.B. Moulton, G.J. Wozniak, B. Cauvin, R.P. Schmitt, J.S. Sventek and L.G. Moretto, Phys. Rev. **C25** (1982) 300
30) L.G. Moretto, S.K. Kataria, R.C. Jared, R. Schmitt and S.G. Thompson, Nucl. Phys. **A255** (1975) 491
31) R. Babinet, L.G. Moretto, J. Galin, R. Jared, J. Moulton and S.G. Thompson Nucl. Phys. **A258** (1976) 172
32) R.P. Schmitt, G. Bizard, G.J. Wozniak and L.G. Moretto, Phys. Rev. Lett. **46** (1981) 522
33) K.T. Davies and A.J. Sierk, Phys. Rev. C31 (1985) 915
34) R. Bass, Nucl. Phys. **A231** (1974) 45
35) R. Bass, Phys. Rev. Lett. 39 (1977) 265
36) R. Vandenbosch and J. Huizenga, "Nuclear Fission", Academic Press, N. Y. (1973) (See Chapters 7, 8)
37) L. G. Moretto and G. J. Wozniak, Prog. in Part. & Nucl. Phys., **21** (1988) 401
38) L. G. Moretto, Physics and Chemistry of Fission, Vol. **1**, I. A. E. A., Vienna (1974), p. 329
39) V.F. Weisskopf and P.H. Ewing, Phy. Rev. **57** (1940) 472
40) B. Haas, G. Duchene, F.A. Beck, T. Byrski, C. Gehringer, J.C. Merdinger, A. Nourredine, V. Rauch, J.P. Vivien, J. Barrette, S. Tobbeche, E. Bozek, J. Styczen, J. Keinonen, J. Dudek and W. Nazarewic, Phys Rev. Lett. **54** (1985) 398
41) A.J. Sierk, private communication
42) M.G. Mustafa, Proceedings of the USSR symposium of physics of Nuclear Fission, June 1987, Voprosy Atomnoi Nauki I Tekhniki, Vol. 1 (1988) p. 75
M.G. Mustafa, UCRL-97081 preprint, July 7 1987

Table Captions

Table 1. Tabulated values of the maximum angular momentum for fusion. The first column contains the bombarding energy per nucleon. The second column contains the L_{max} values predicted by the Bass model. In the third and fourth columns are the values used in Gemini and in the fits, respectively.

Table 2. Tabulated values of the finite range, liquid drop and experimental barriers (in MeV) and the ratio of the level density parameters as determined from the fitting procedure. The errors shown are those arising from the χ^2 of the fitting procedure. To these values an overall systematic error of the order of $\pm$ 3.5% is be assigned as discussed in the text.

Table 1.

Energy (MeV/A)	Bass ($\hbar$)	Fits ($\hbar$)	Gemini ($\hbar$)
12.7	42.9	42	42
10.2	42.9	39	39
8.0	39.3	37	36
6.9	36.5	35	34
6.2	34.6	32	33
5.0	30.3	30	30

Table 2.

Z	F.R. (MeV)	L.D. (MeV)	Exper. (MeV)	$R=a_z/a_n$
5	25.7	42.0	27.3 ± 1.1	.956 ± .034
6	27.8	44.0	26.4 ± 1.1	.952 ± .034
7	29.9	45.4	29.8 ± 1.1	.929 ± .034
8	31.8	46.4	30.3 ± 1.1	.919 ± .032
9	33.0	47.9	32.9 ± 1.2	.906 ± .032
10	34.1	48.5	33.4 ± 1.2	.902 ± .032
11	35.0	48.9	34.3 ± 1.2	.900 ± .032
12	35.9	49.6	36.0 ± 1.2	.923 ± .032
13	36.4	49.9	35.6 ± 1.2	.900 ± .032
14	36.8	50.1	35.7 ± 1.2	.900 ± .032
15	37.0	50.3	37.4 ± 1.3	.913 ± .032
16	37.1	50.4	36.9 ± 1.3	.900 ± .032
17	37.2	50.5	37.8 ± 1.3	.910 ± .032
18	37.2	50.5	37.5 ± 1.3	.904 ± .032
19	37.1	50.4	37.8 ± 1.3	.913 ± .032
20	37.0	50.3	37.5 ± 1.3	.917 ± .032
21	36.8	50.1	37.1 ± 1.3	.916 ± .034
22	36.4	49.9	36.6 ± 1.3	.921 ± .034
23	35.9	49.6	36.7 ± 1.3	.941 ± .035
24	35.0	48.9	35.1 ± 1.2	.939 ± .035
25	34.1	48.5	35.8 ± 1.2	.986 ± .035
26	33.0	47.9	33.3 ± 1.2	.977 ± .035

Figure Captions

1. Schematic potential-energy surface as a function of the reaction and mass-asymmetry coordinates.

2. Schematic ridge-line potentials (solid curves) and expected yields (dashed curves) as a function of the mass-asymmetry coordinate for: a) a heavy system above and b) a light system below the Businaro-Gallone point.

3. Fission symmetric barriers of nonrotating nuclei as a function of Z^2/A, along the line of beta stability. The upper line represents the results of calculations with liquid-drop model parameters. The lower line represents the results from the finite range model. Both calculations use the two-center model shapes. (Ref. 42)

4. Liquid drop (RLDM) and rotating finite range model (RFRM) calculations incorporating the effects of the finite range of the nuclear force and surface diffuseness for ^{75}Br. The result is a substantial reduction in the fission barriers, B(J), compared with the prediction of the RLDM.

5. Density plots of ΔE vs E for the reaction 10.2 MeV/A $^{63}Cu + ^{12}C$ for fragments detected at forward laboratory angles.

6. Schematic representation of the reverse kinematics production of a compound-nucleus and its decay by fragment emission (see text).

7. Contours of the experimental cross section $\partial^2\sigma/\partial V_\perp V_\parallel$ in the $V_\perp$ - $V_\parallel$ plane for representative Z-values detected in the reaction 6.9 MeV/A $^{63}Cu + ^{12}C$. The fragment velocities are expressed as a fraction of the beam velocity and the beam direction is vertical. The magnitudes of the contour levels indicated are relative.

8. Same as in Fig. 7 for Z = 10, 15, 20 at the four highest bombarding energies.

9. In the upper part of each section, are shown the source velocities (x's) extracted from the invariant cross section plots for each Z-species produced in the 6.9, 8.0, 10.2 and 12.7 MeV/A $^{63}Cu + ^{12}C$ reactions. The single large error bar for each data set indicates the possible systematic error due to the mass parameterization and energy calibrations. The complete fusion velocity (V_{cf}) is also shown in the plot and indicated by the horizontal line. In the lower portion of the figure, are shown the extracted Coulomb velocities (diamonds).

For comparison a calculation based on the Viola systematics (solid lines) and GEMINI (dashed line) is also shown. The experimental and calculated variances of the velocity distributions are shown by the open squares and stars, respectively.

10. Smoothed experimental kinetic energy spectra in the center of mass for boron (Z=5) fragments emitted in the reaction E/A = 6.9 MeV $^{63}Cu + ^{12}C$.

11.Smoothed kinetic energy spectra for representative Z-values for the isotropic component measured in the E/A = 8.0 MeV $^{63}Cu + ^{12}C$ reaction.

12. The first (Xs) and second (crosses) moments of the fragment center-of-mass kinetic energies are shown for the 6.9, 8.0, 10.2, 12.7 MeV/A $^{63}Cu + ^{12}C$ reactions. The solid lines show the calculated Coulomb repulsion energies between two touching spheres which is discussed in the text. The first (diamonds) and second (squares) moments of the fragment center-of-mass kinetic energies calculated by GEMINI are shown also.

13. Angular distributions $d\sigma/d\theta$ in the frame of the source system for representative Z-values produced in the 12.7 and 10.2 MeV/A $^{63}Cu + ^{12}C$ reactions.

14. Same as in Fig. 13 for the 8.0 and 6.9 MeV/A $^{63}Cu + ^{12}C$ reactions.

15. Comparison of experimental (diamonds) and calculated (lines) charge distributions for the $^{63}Cu + ^{12}C$ reaction at six bombarding energies. The statistical errors are indicated when they are larger than the experimental data points. Also shown are the L_{max} values used in the GEMINI calculations for each bombarding energy.

16. Dependence of the total integrated cross section on the center-of-mass energy for emission of complex fragments from the reaction $^{63}Cu + ^{12}C$. The points and error bars correspond to the experimental cross sections with statistical errors. The curves are fits with the parameters shown in Fig. 19. The numbers to the right indicate the factor by which each curve and set of experimental points was multiplied by in order to separate it from its neighboring curves for visual display purposes.

17. The relative yield of coincidence events plotted as function of the sum of the atomic charges of the two coincident fragments for the E = 12.7, 8.0, 6.9, 6.2 MeV/A $^{63}Cu + ^{12}C$ reactions. For each bombarding energy, the mean total detected charge is given.

18. Comparison of experimental and calculated charge distributions for six bombarding energies. The experimental data are indicated by the diamonds with their respective statistical error. The calculated values from the fits are shown by the solid line. Also shown are the L_{max} values used in the fits.

19. The experimental emission barriers (solid points) and ratio (x's) of the level density parameters, extracted in fitting the excitation functions as a function of the fragment charge or asymmetry, Z/Z_{cn} ($Z/Z_{cn} = 0.5$ corresponds to symmetric splitting). The error bars arising from the $\chi 2$ of the fitting procedure are smaller than the size of the points. The large error bar represents an estimate of the possible systematic errors as discussed in the text. The predicted barriers from the finite range model and the liquid drop model are shown by the solid and dashed lines, respectively.

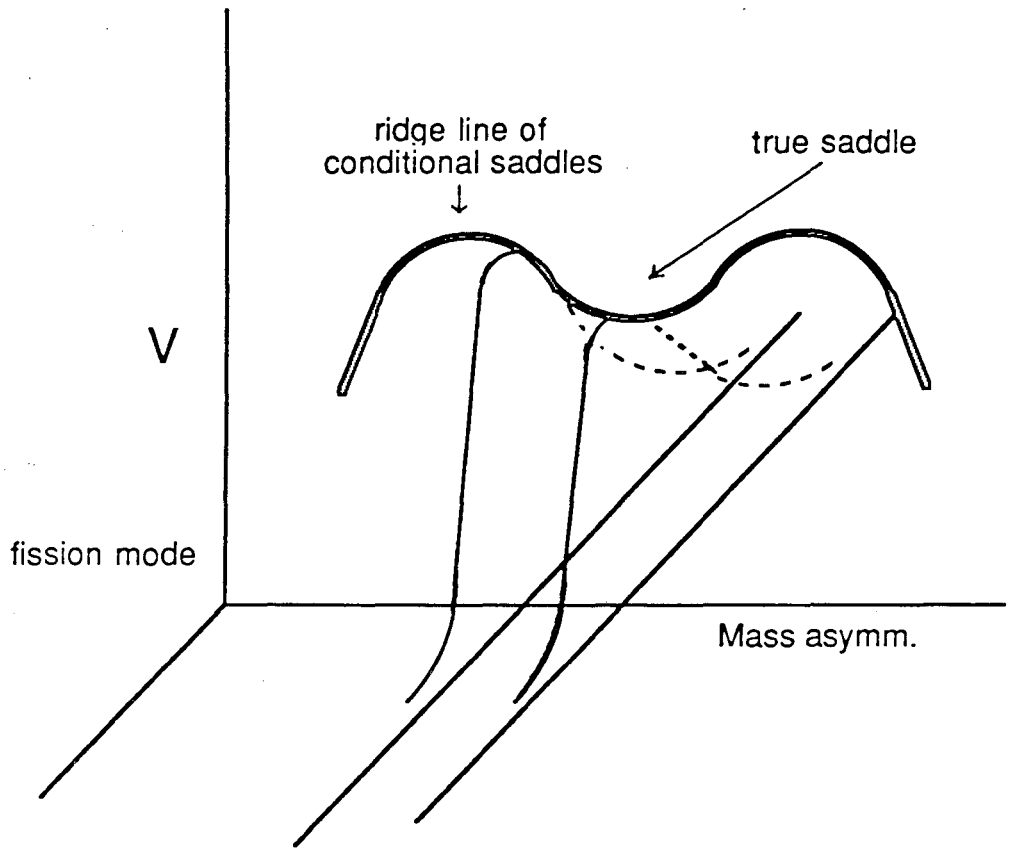

XBL 868-3111

Figure 1

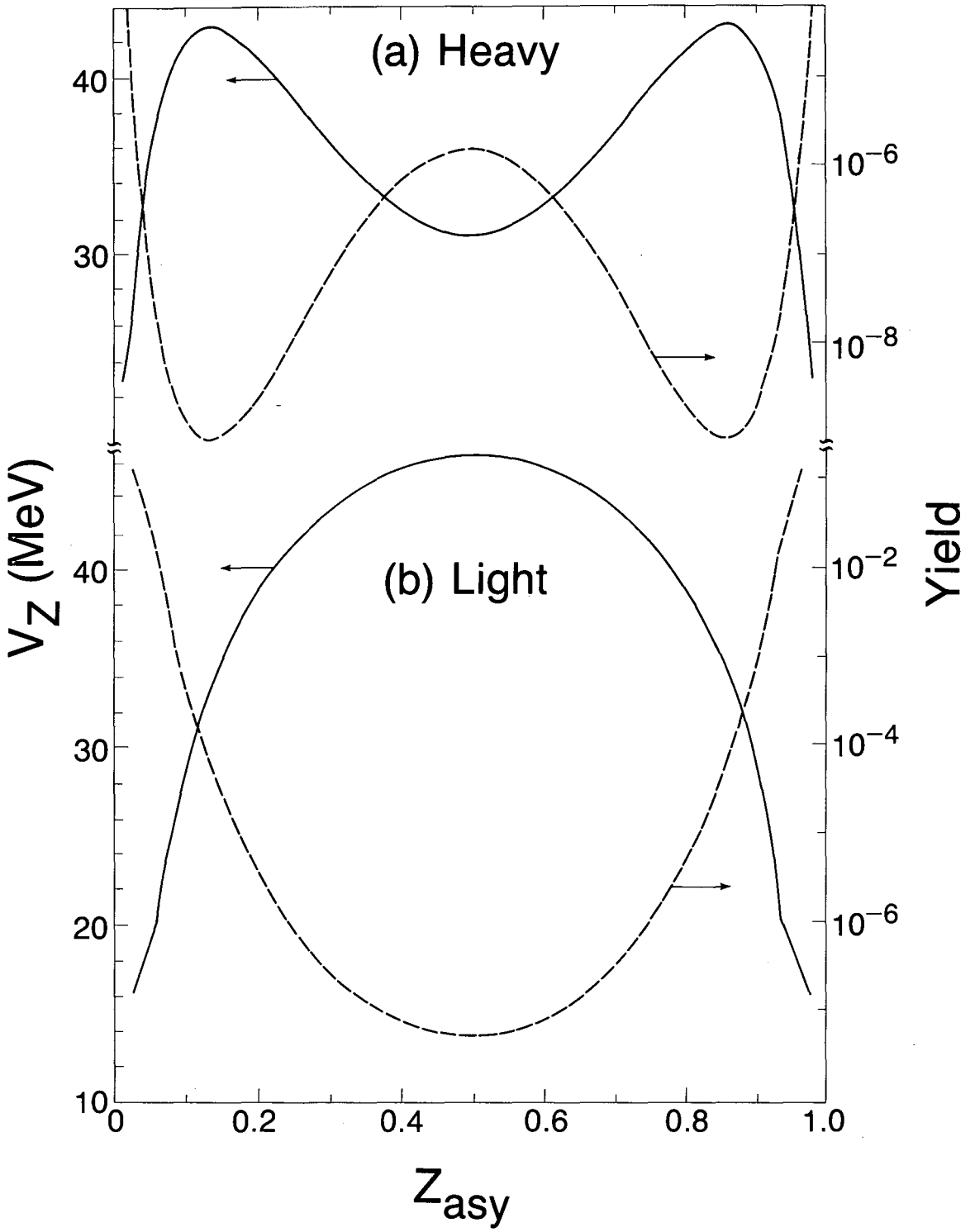

XBL 847-10685A

Figure 2

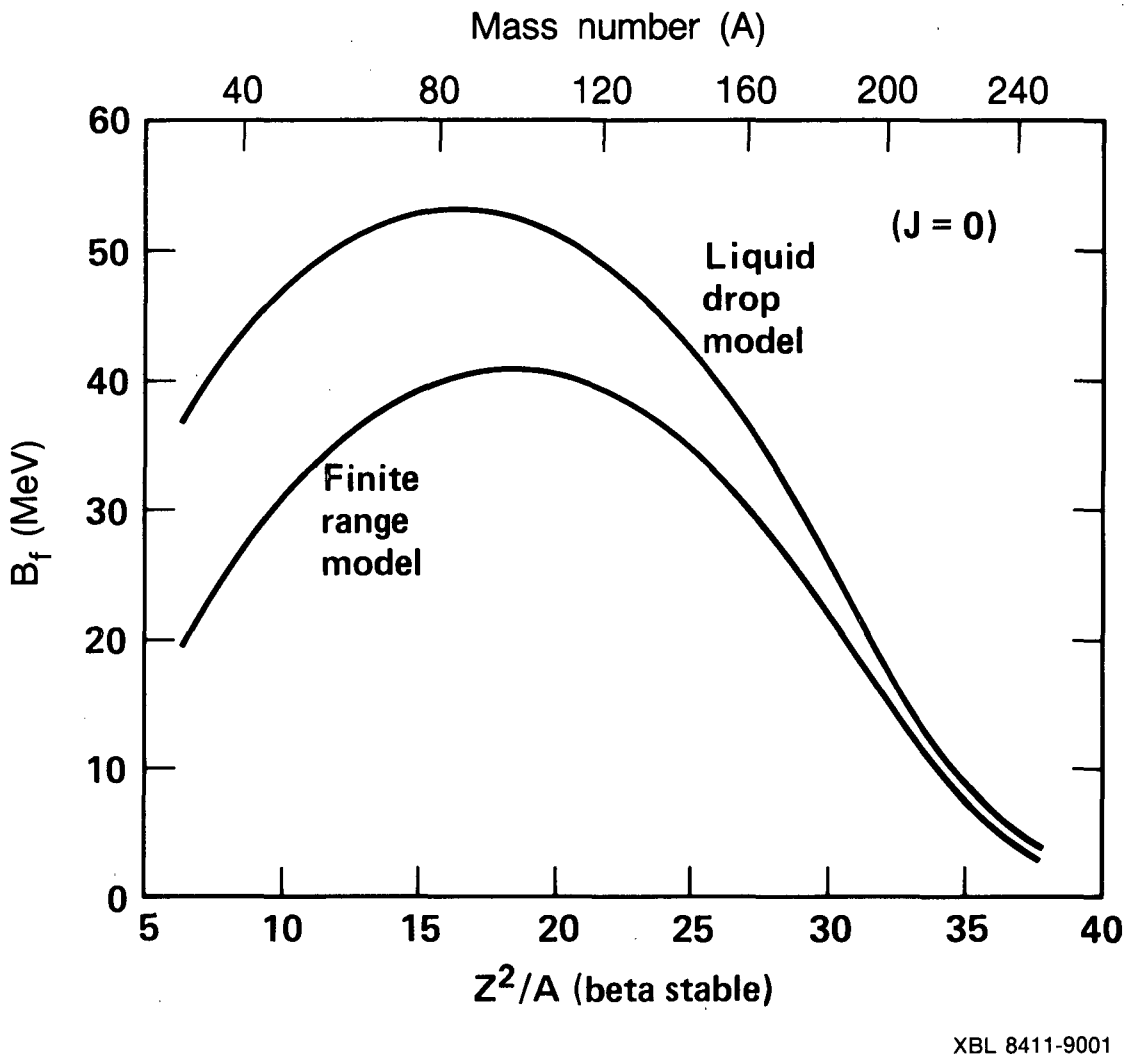
Mass number (A)
40
80
120
160
200
240
60
50
40
30
20
10
0
B_f (MeV)
(J = 0)
Liquid drop model
Finite range model
5
10
15
20
25
30
35
40
Z^2/A (beta stable)
XBL 8411-9001

Figure 3

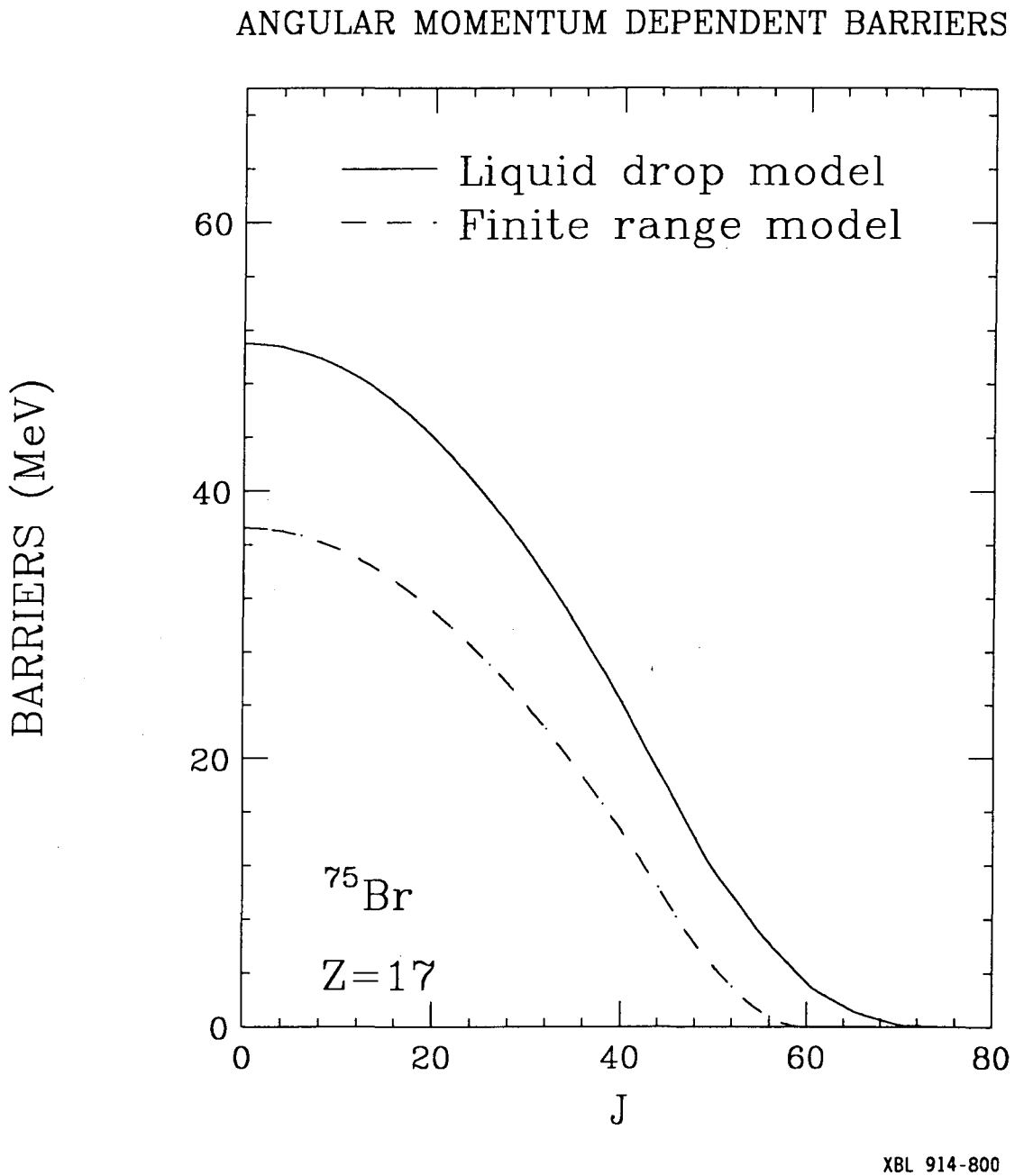
ANGULAR MOMENTUM DEPENDENT BARRIERS
Liquid drop model
Finite range model
BARRIERS (MeV)
60
40
20
0
0
20
40
60
80
J
^{75}Br
Z=17
XBL 914-800

Figure 4

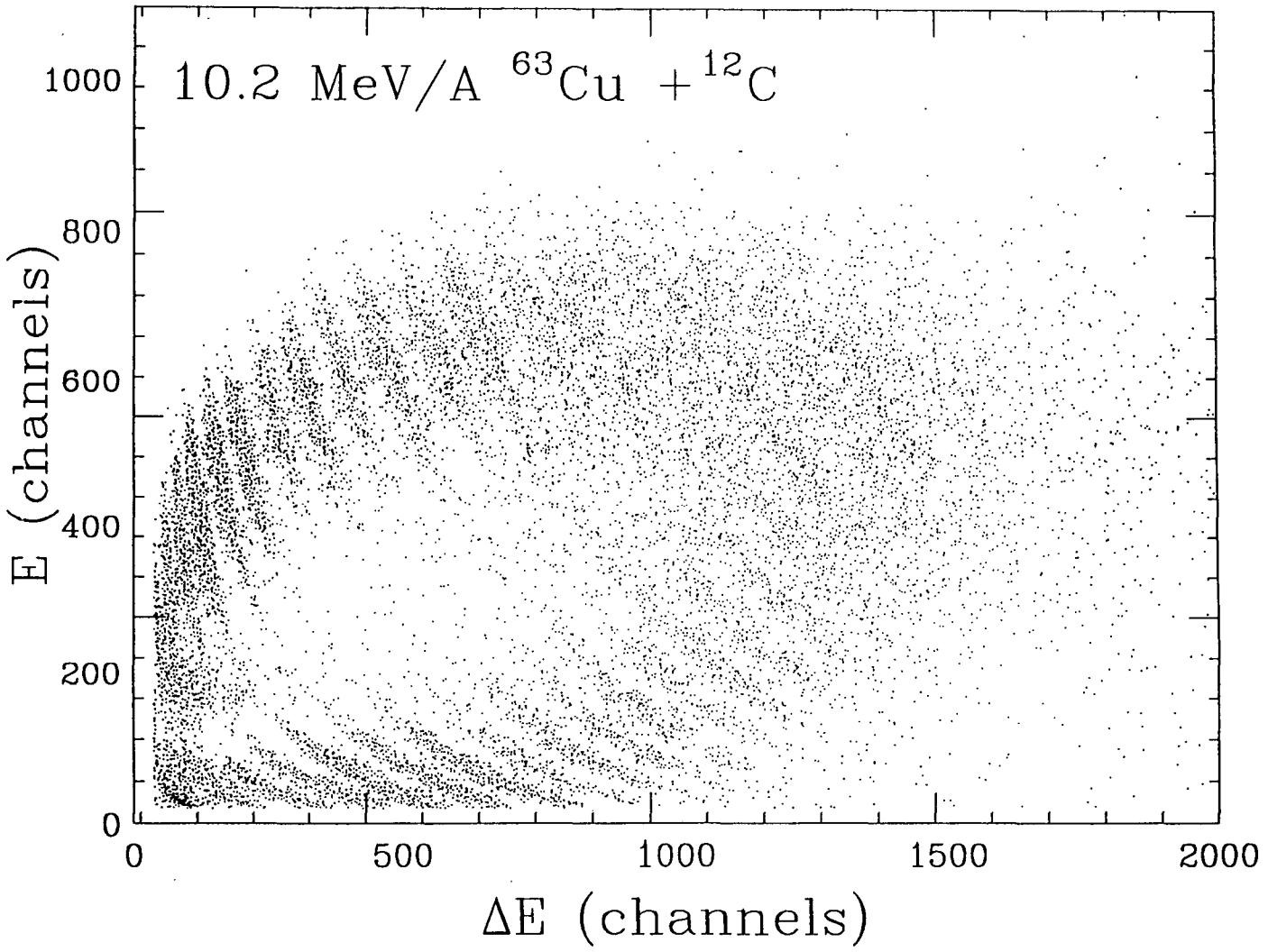

XBL 914-791

Figure 5

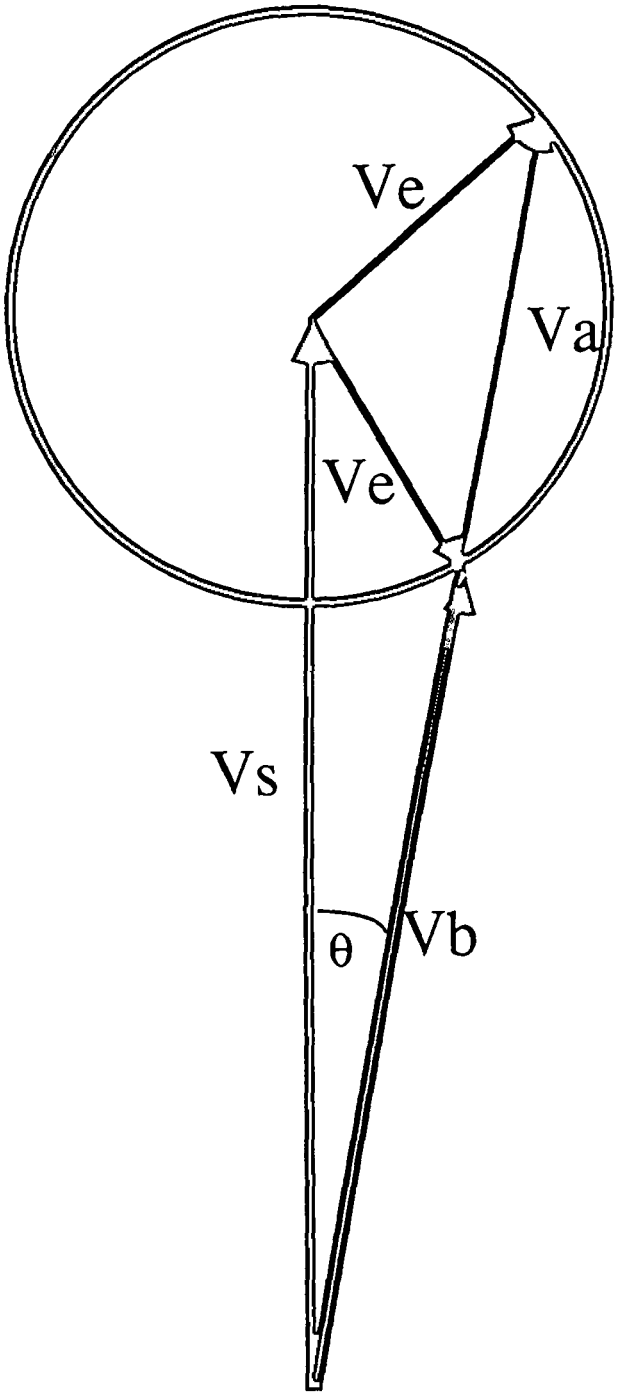

XBL 914-805

Figure 6

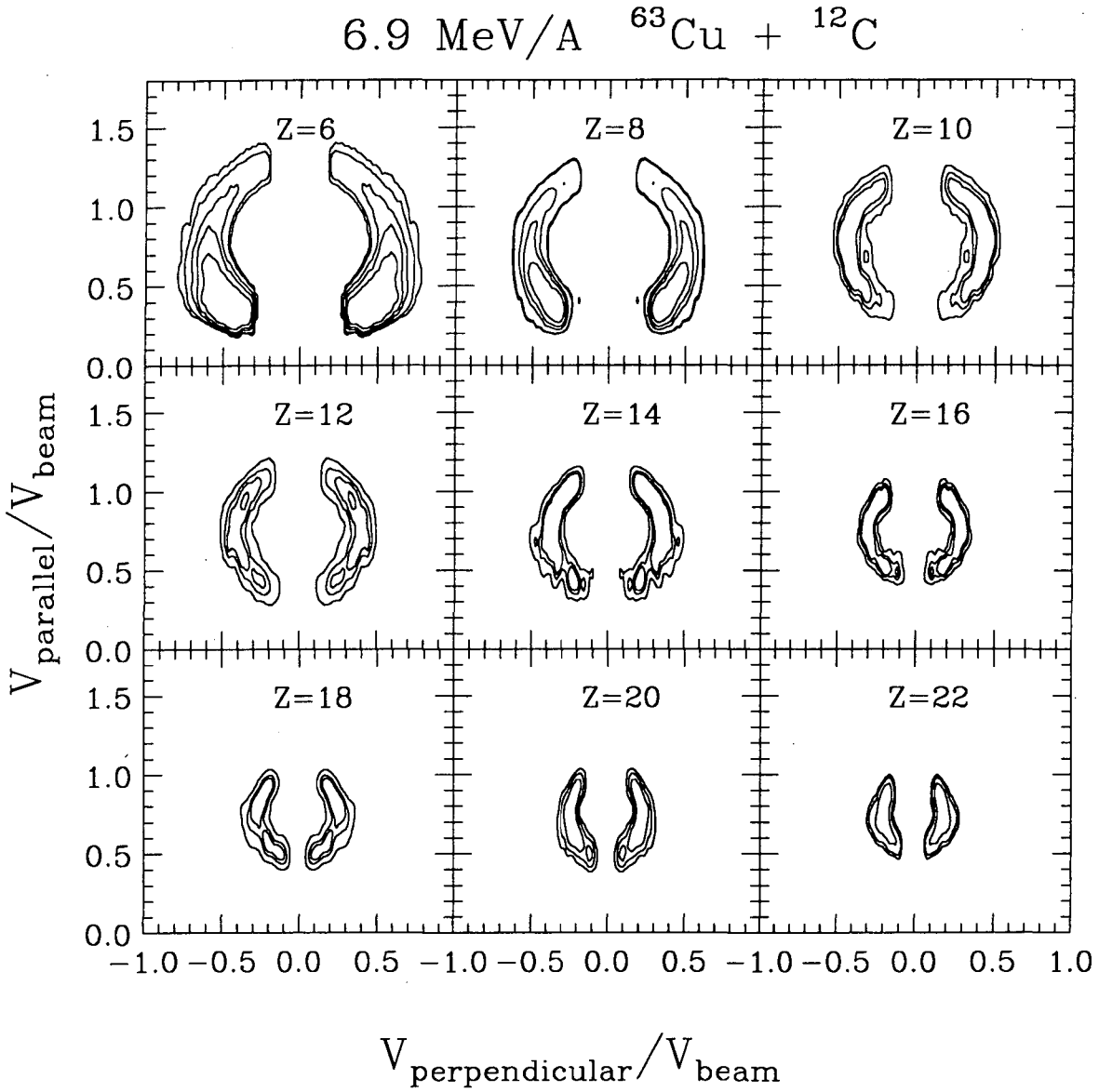
6.9 MeV/A ^{63}Cu + ^{12}C
Z=6
Z=8
Z=10
Z=12
Z=14
Z=16
Z=18
Z=20
Z=22
1.5
1.0
0.5
0.0
−1.0 −0.5 0.0 0.5 −1.0 −0.5 0.0 0.5 −1.0 −0.5 0.0 0.5 1.0
$V_{parallel}/V_{beam}$
$V_{perpendicular}/V_{beam}$
XBL 914-801

Figure 7

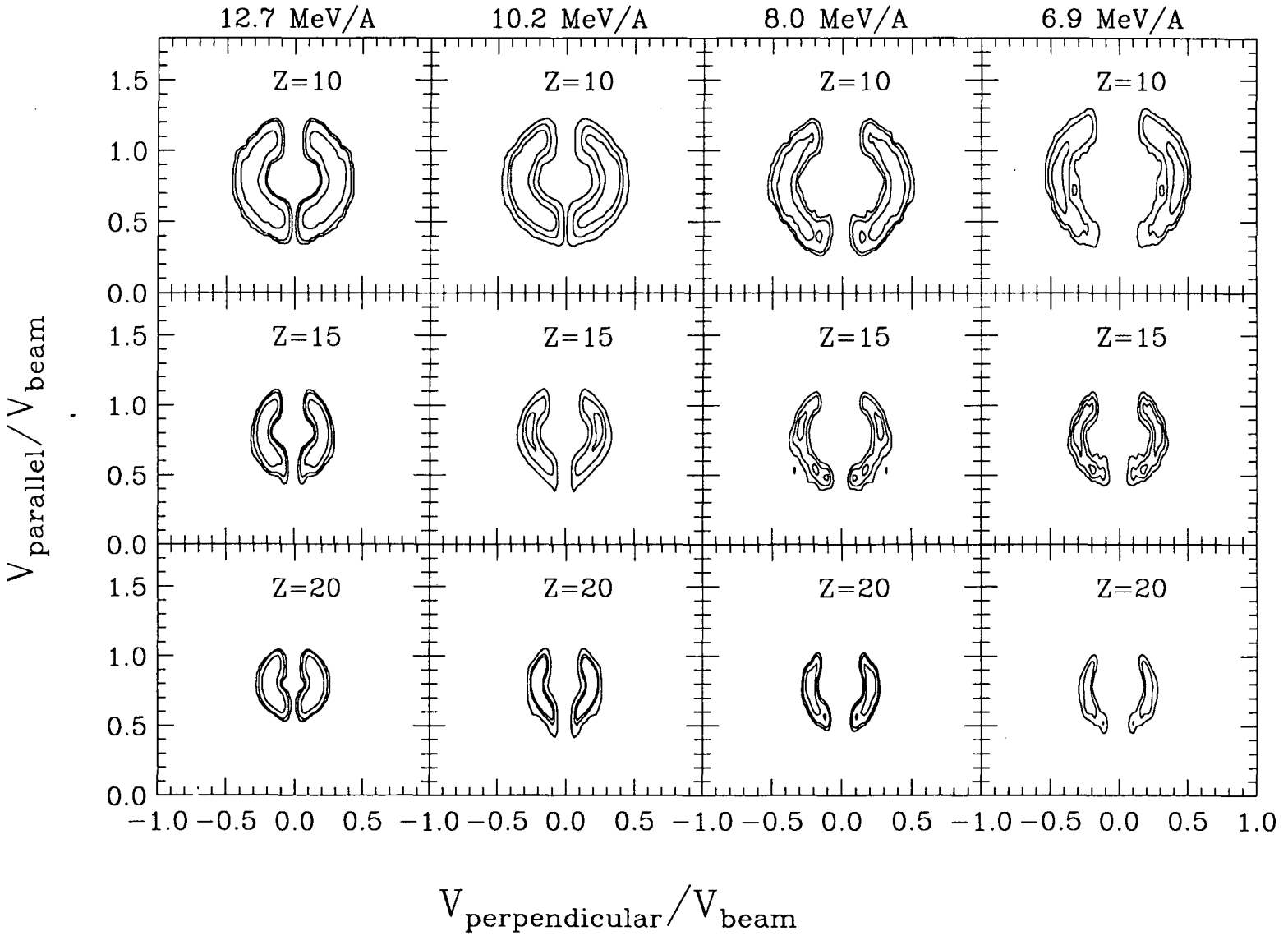

Figure 8

XBL 914-790

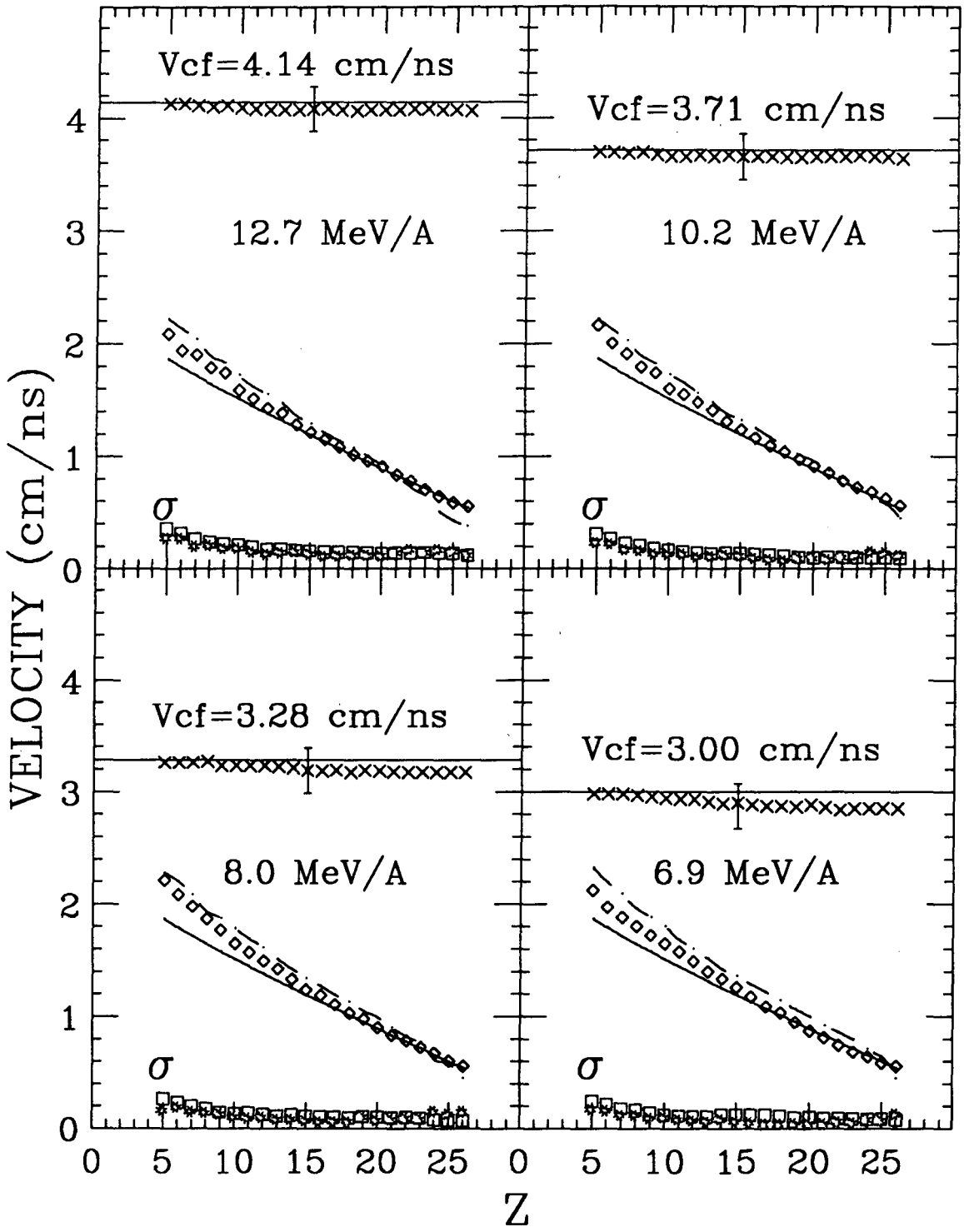

XBL 914-910

Figure 9

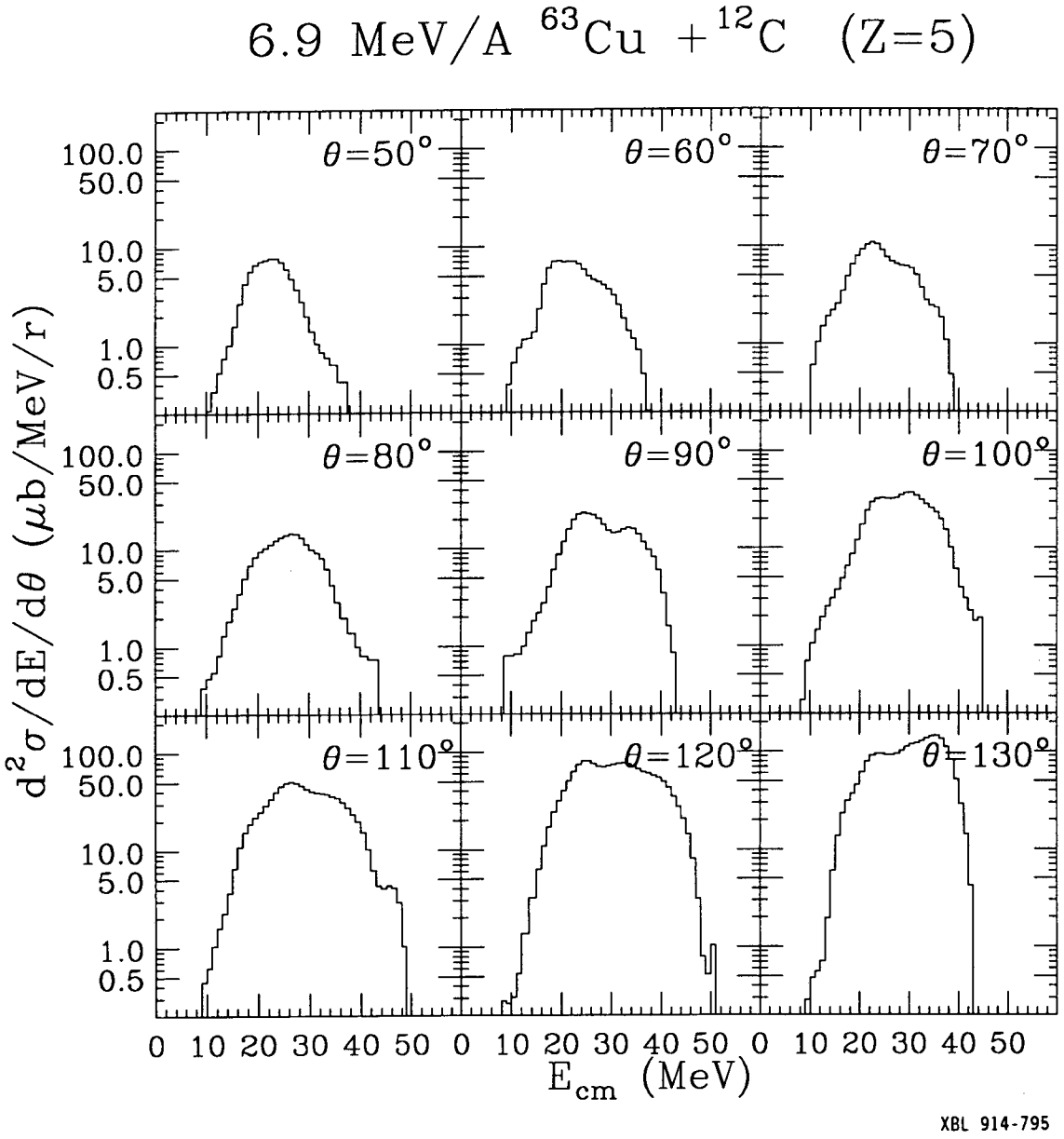
6.9 MeV/A ^{63}Cu + ^{12}C (Z=5)
θ=50°
θ=60°
θ=70°
θ=80°
θ=90°
θ=100°
θ=110°
θ=120°
θ=130°
100.0
50.0
10.0
5.0
1.0
0.5
d²σ/dE/dθ (μb/MeV/r)
0 10 20 30 40 50
E_cm (MeV)
XBL 914-795

Figure 10

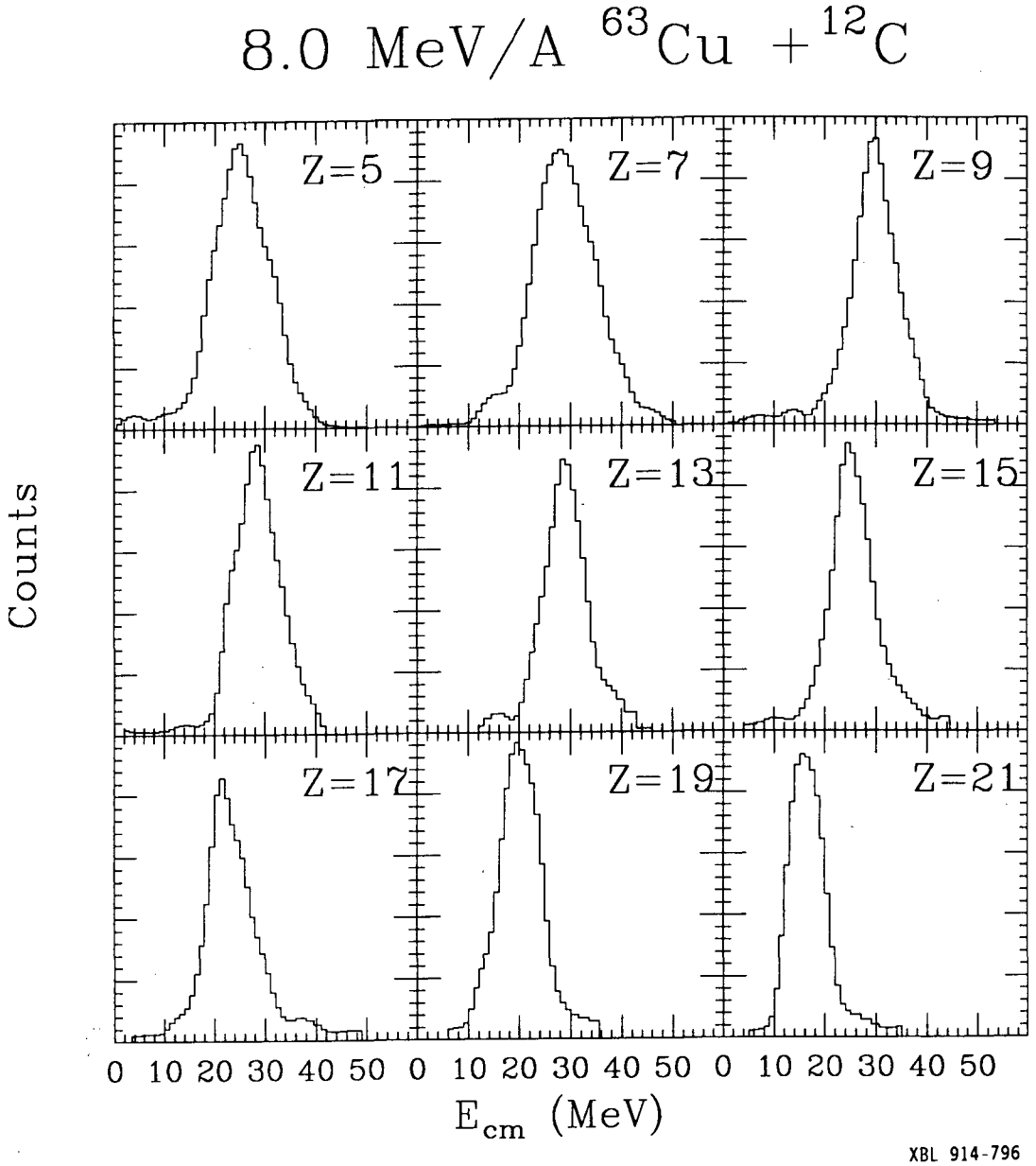
8.0 MeV/A ^{63}Cu + ^{12}C
Z=5
Z=7
Z=9
Z=11
Z=13
Z=15
Z=17
Z=19
Z=21
Counts
0 10 20 30 40 50 0 10 20 30 40 50 0 10 20 30 40 50
E_{cm} (MeV)
XBL 914-796

Figure 11

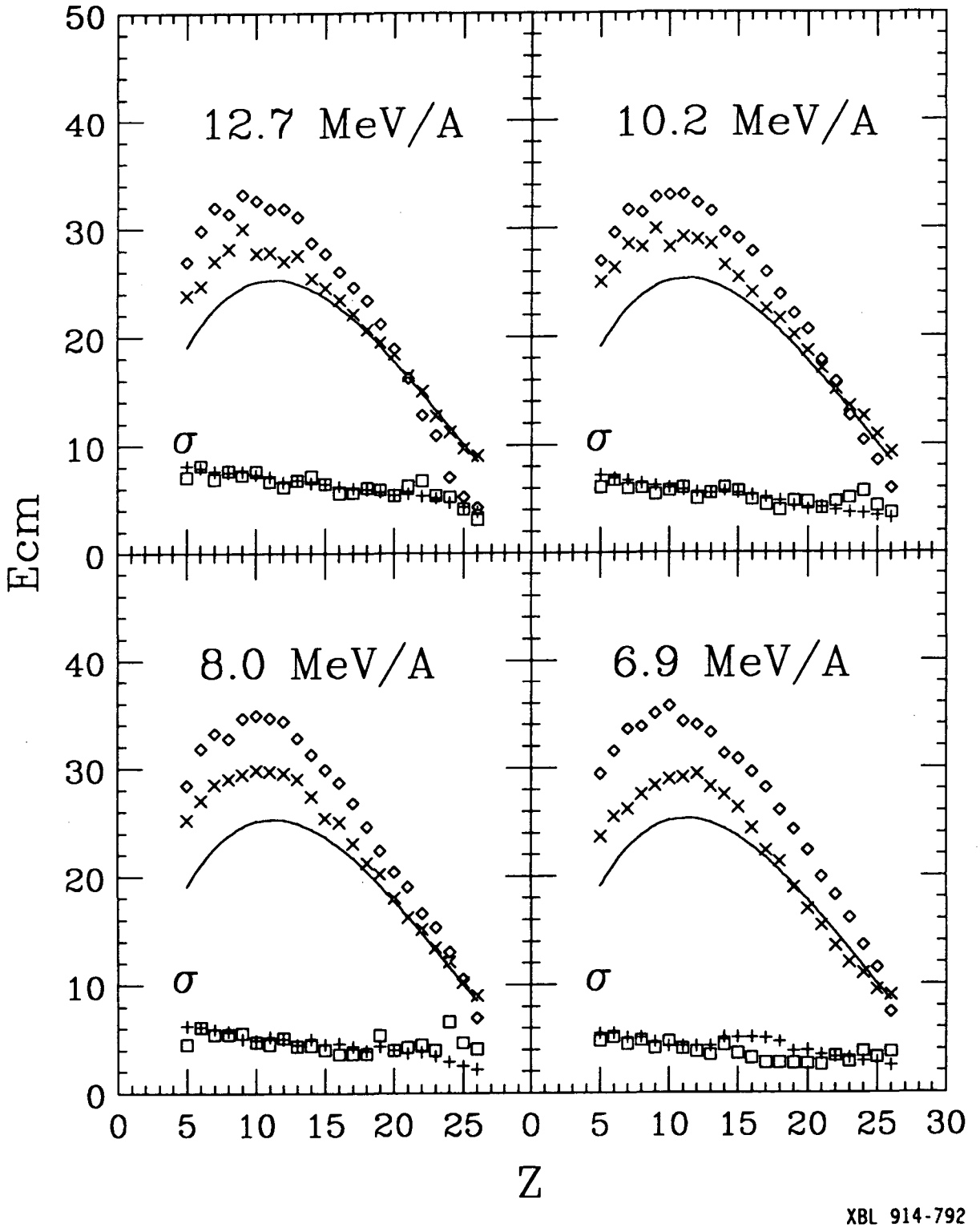

Figure 12

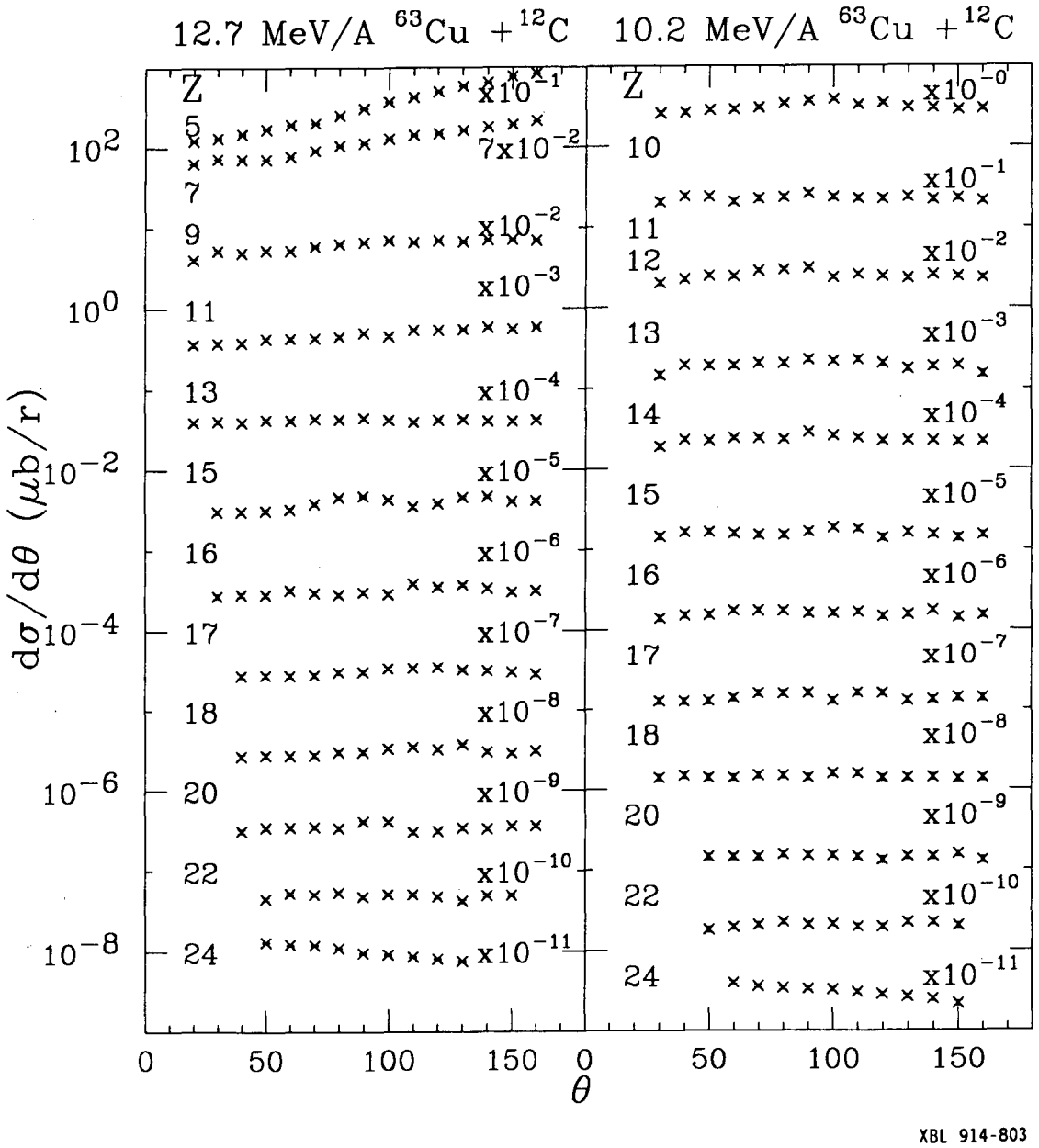
12.7 MeV/A ^{63}Cu + ^{12}C
10.2 MeV/A ^{63}Cu + ^{12}C
Z
5
7
9
11
13
15
16
17
18
20
22
24
x10^{-1}
7x10^{-2}
x10^{-2}
x10^{-3}
x10^{-4}
x10^{-5}
x10^{-6}
x10^{-7}
x10^{-8}
x10^{-9}
x10^{-10}
x10^{-11}
Z
10
11
12
13
14
15
16
17
18
20
22
24
x10^{-0}
x10^{-1}
x10^{-2}
x10^{-3}
x10^{-4}
x10^{-5}
x10^{-6}
x10^{-7}
x10^{-8}
x10^{-9}
x10^{-10}
x10^{-11}
10^2
10^0
10^{-2}
10^{-4}
10^{-6}
10^{-8}
$d\sigma/d\theta$ (μb/r)
0
50
100
150
0
50
100
150
θ
XBL 914-803

Figure 13

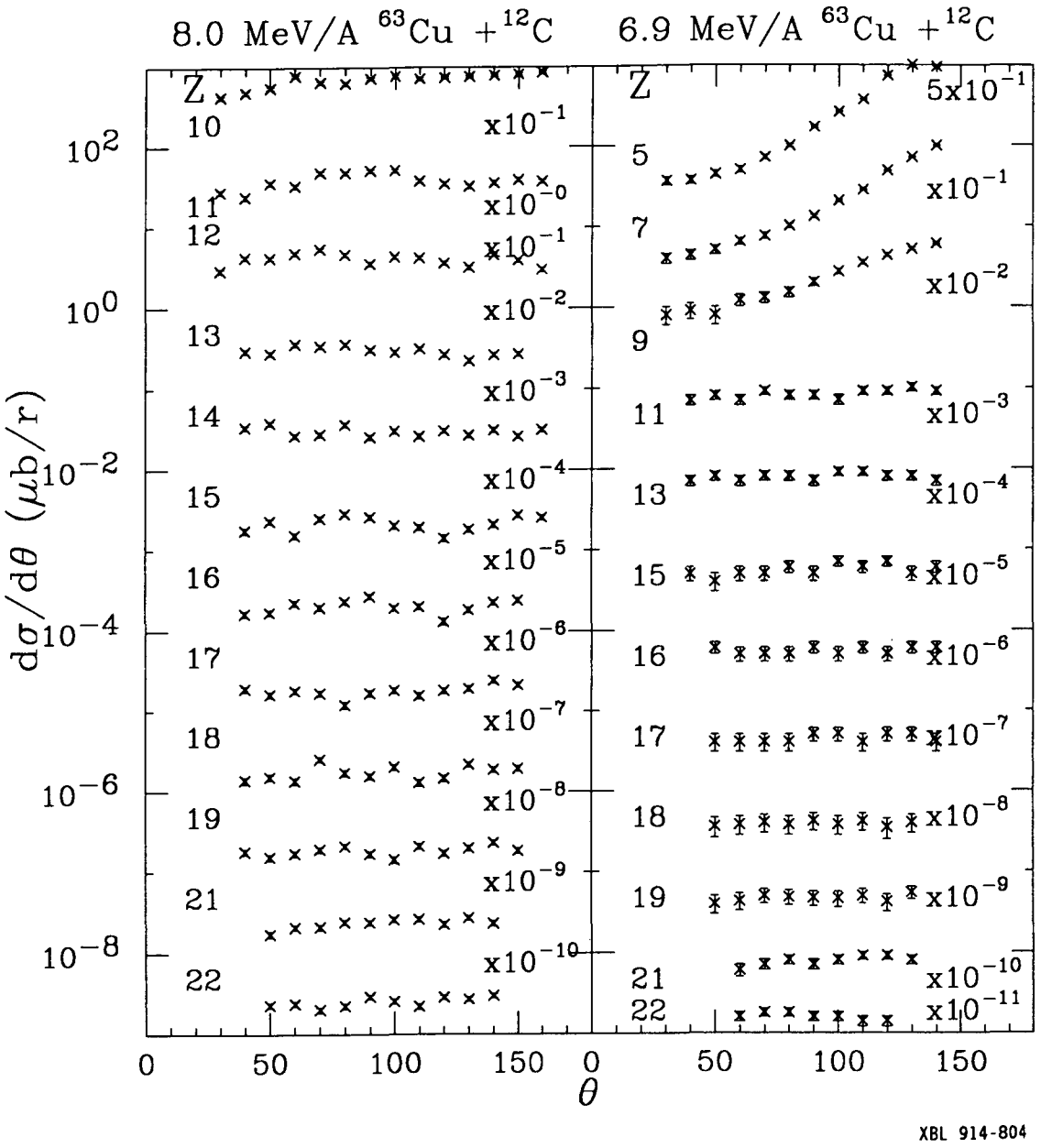
8.0 MeV/A ^{63}Cu + ^{12}C
6.9 MeV/A ^{63}Cu + ^{12}C
Z
10
11
12
13
14
15
16
17
18
19
21
22
x10^{-1}
x10^{-0}
x10^{-1}
x10^{-2}
x10^{-3}
x10^{-4}
x10^{-5}
x10^{-6}
x10^{-7}
x10^{-8}
x10^{-9}
x10^{-10}
5
7
9
11
13
15
16
17
18
19
21
22
5x10^{-1}
x10^{-1}
x10^{-2}
x10^{-3}
x10^{-4}
x10^{-5}
x10^{-6}
x10^{-7}
x10^{-8}
x10^{-9}
x10^{-10}
x10^{-11}
$d\sigma/d\theta$ (μb/r)
10^2
10^0
10^{-2}
10^{-4}
10^{-6}
10^{-8}
0
50
100
150
θ
XBL 914-804

Figure 14

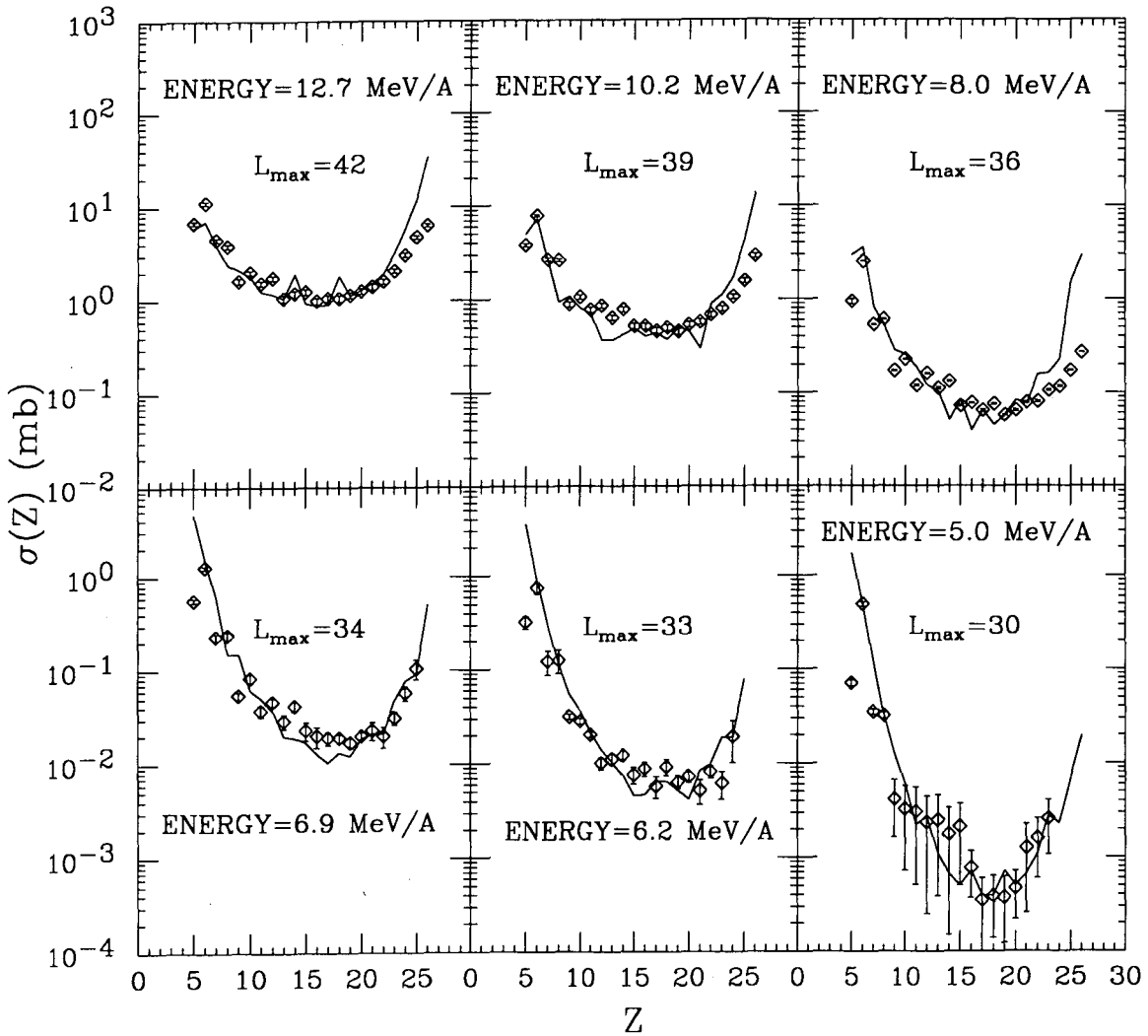
ENERGY=12.7 MeV/A
L_{max}=42
ENERGY=10.2 MeV/A
L_{max}=39
ENERGY=8.0 MeV/A
L_{max}=36
ENERGY=6.9 MeV/A
L_{max}=34
ENERGY=6.2 MeV/A
L_{max}=33
ENERGY=5.0 MeV/A
L_{max}=30
σ(Z) (mb)
Z
XBL 914-789

Figure 15

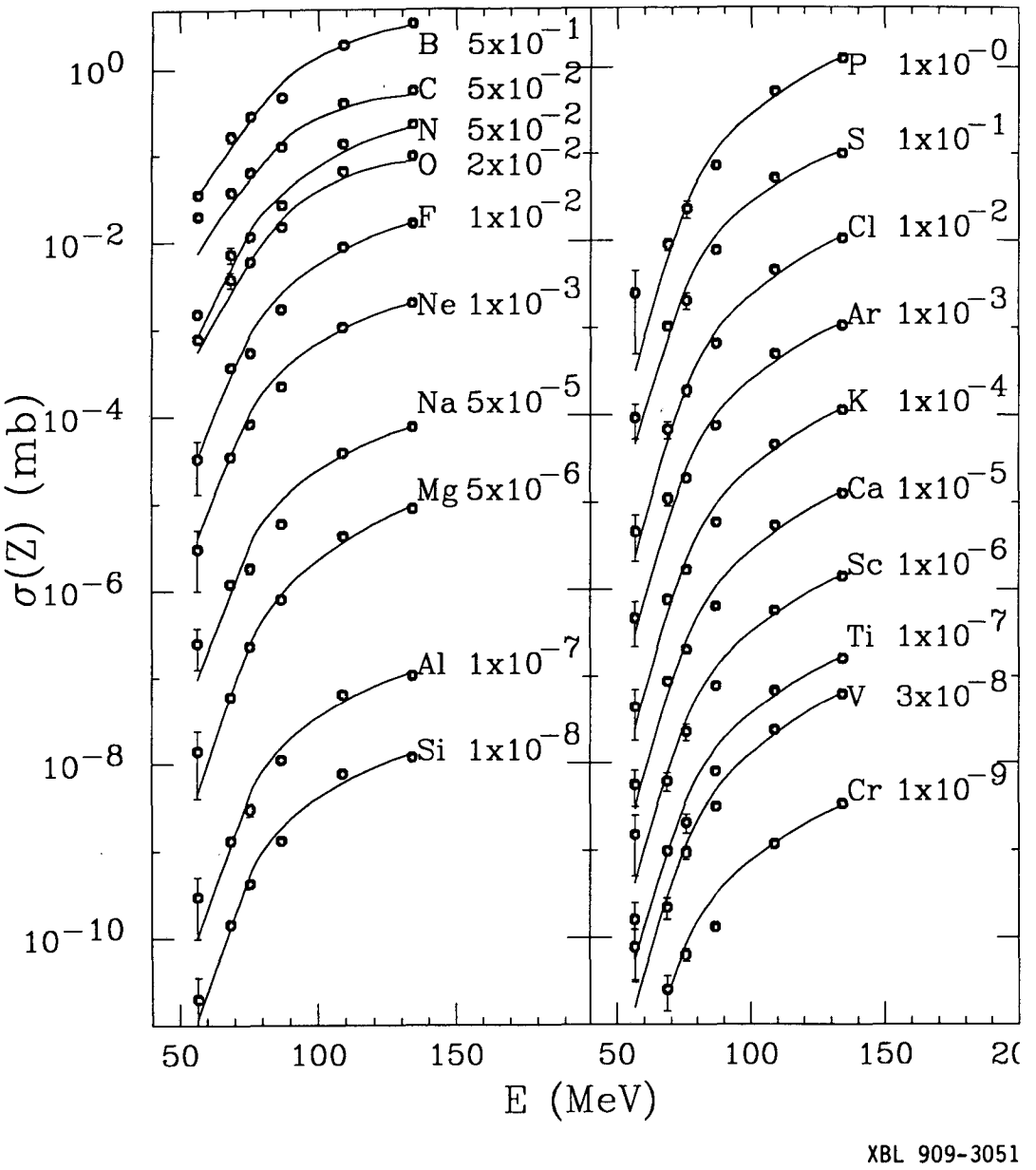
B 5x10^-1
C 5x10^-2
N 5x10^-2
O 2x10^-2
F 1x10^-2
Ne 1x10^-3
Na 5x10^-5
Mg 5x10^-6
Al 1x10^-7
Si 1x10^-8
P 1x10^-0
S 1x10^-1
Cl 1x10^-2
Ar 1x10^-3
K 1x10^-4
Ca 1x10^-5
Sc 1x10^-6
Ti 1x10^-7
V 3x10^-8
Cr 1x10^-9
σ(Z) (mb)
E (MeV)
XBL 909-3051

Figure 16

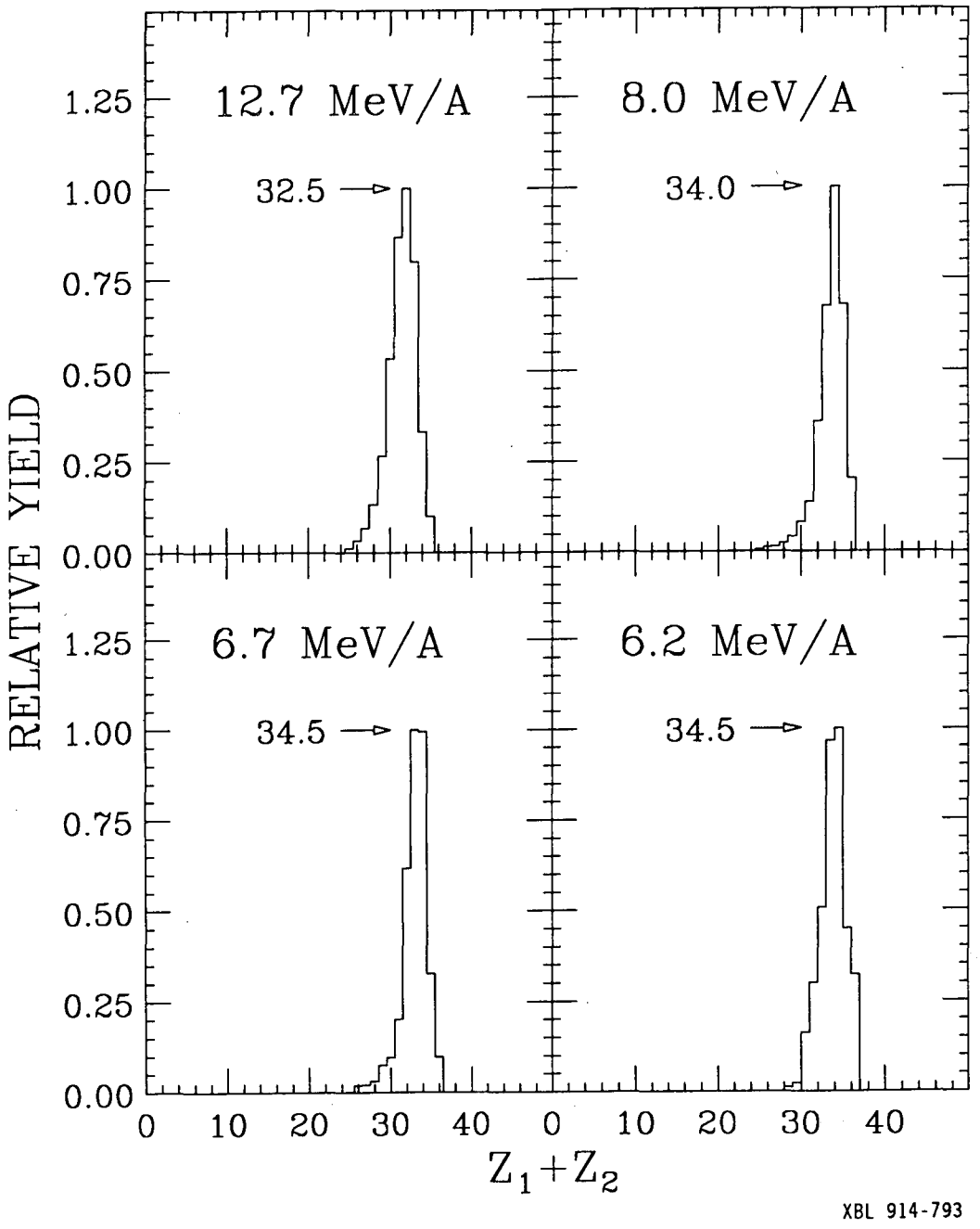
12.7 MeV/A
8.0 MeV/A
6.7 MeV/A
6.2 MeV/A
32.5
34.0
34.5
34.5
RELATIVE YIELD
1.25
1.00
0.75
0.50
0.25
0.00
0
10
20
30
40
Z_1+Z_2
XBL 914-793

Figure 17

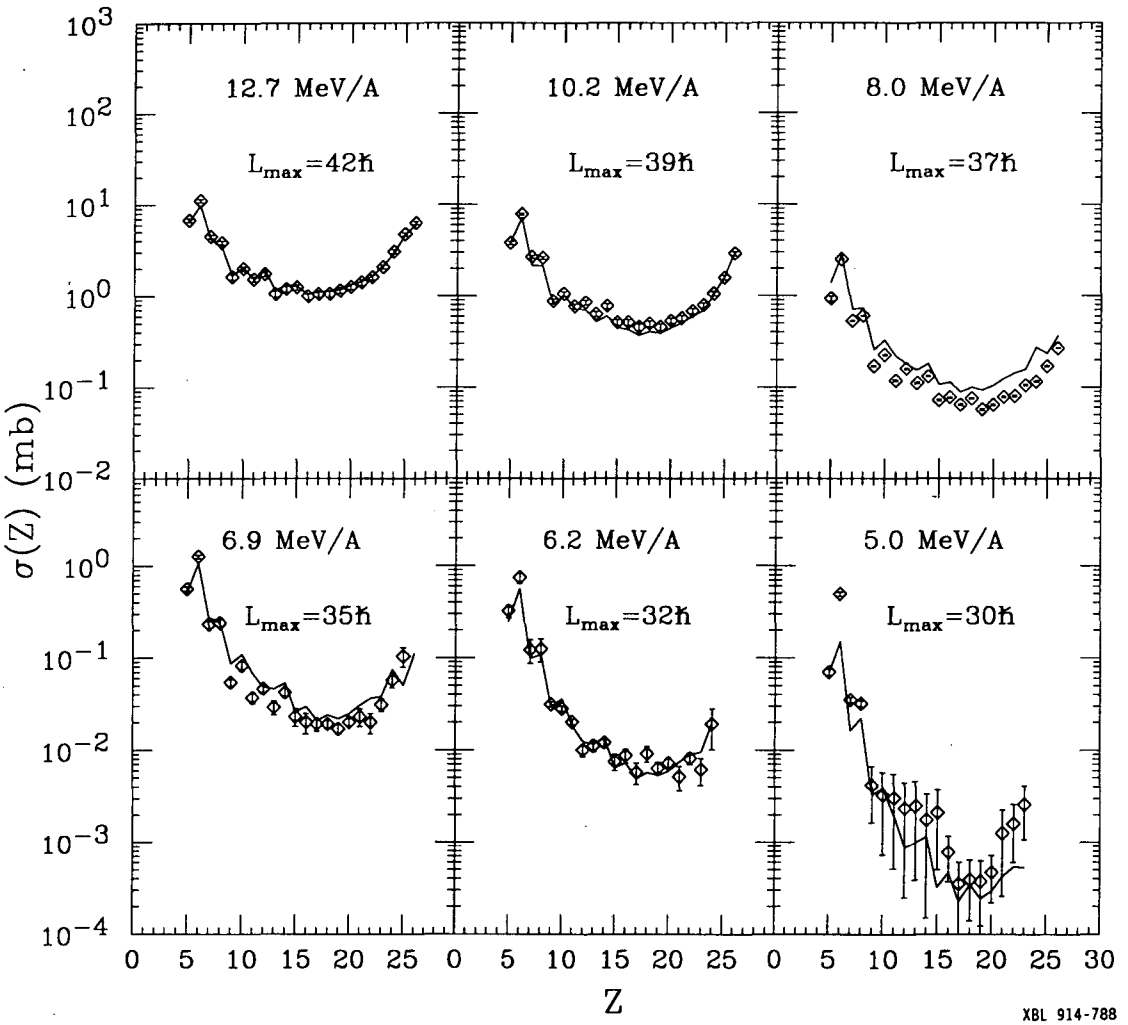
12.7 MeV/A
L_{max}=42ħ
10.2 MeV/A
L_{max}=39ħ
8.0 MeV/A
L_{max}=37ħ
6.9 MeV/A
L_{max}=35ħ
6.2 MeV/A
L_{max}=32ħ
5.0 MeV/A
L_{max}=30ħ
σ(Z) (mb)
Z
XBL 914-788

Figure 18

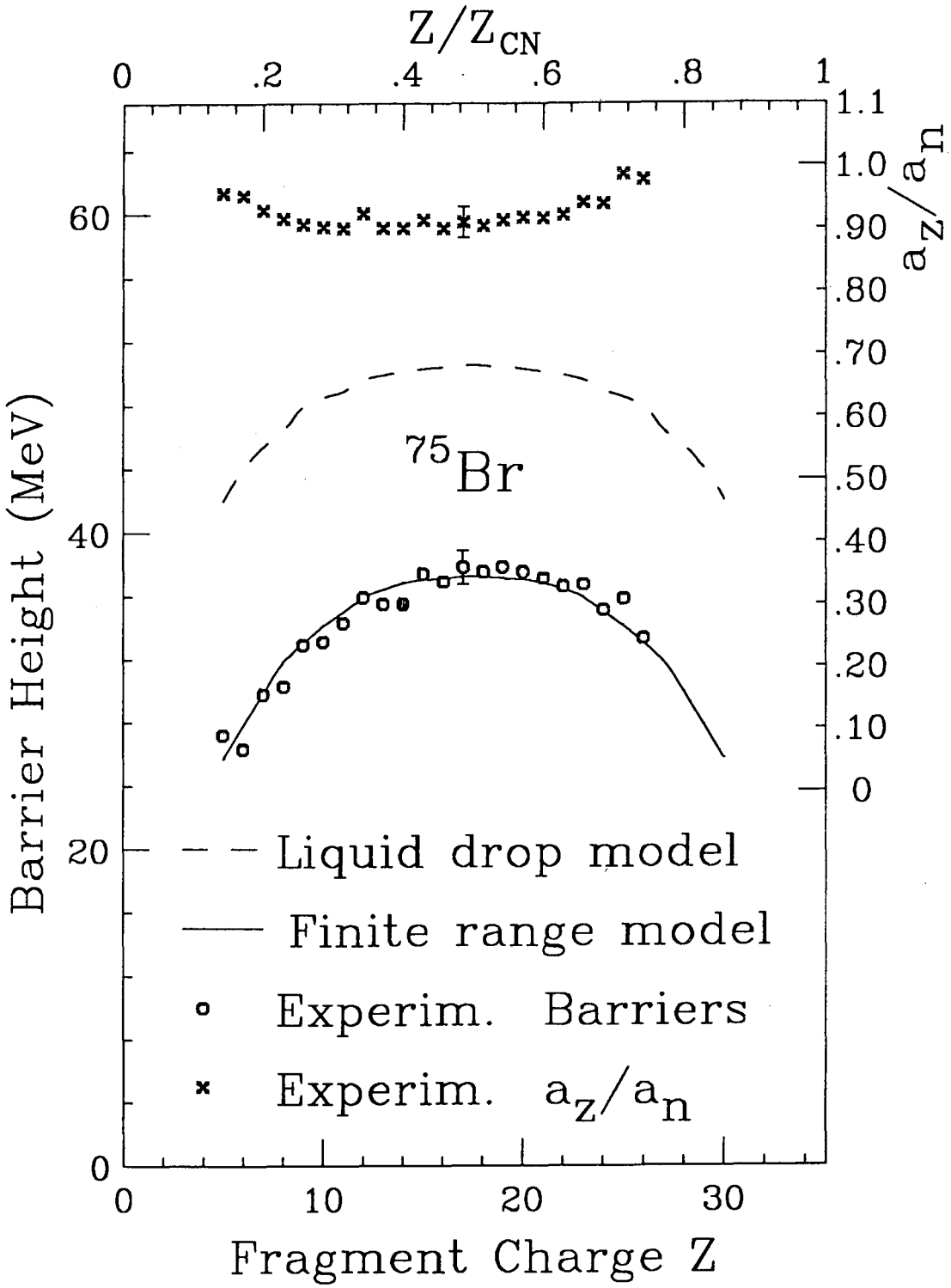

XBL 909-3050

Figure 19

LAWRENCE BERKELEY LABORATORY
UNIVERSITY OF CALIFORNIA
INFORMATION RESOURCES DEPARTMENT
BERKELEY, CALIFORNIA 94720